The Astrophysical Journal, 842:4 (24pp), 2017 June 10 https://doi.org/10.3847/1538-4357/aa6fa9

The Origin of [C II] 157 μm Emission in a Five-component Interstellar Medium: The Case of NGC 3184 and NGC 628

A. Abdullah[1], B. R. Brandl[1,2], B. Groves[3], M. Wolfire[4], D. Calzetti[5], K. Croxall[6], I. de Looze[7,8,9], R. C. Kennicutt[9], K. M. Sandstrom[10], L. Armus[11], D. A. Dale[12], M. Galametz[13], R. Herrera-Camus[14,15], L. K. Hunt[16], J. D. Smith[17], and A. G. G. M. Tielens[1]

[1] Leiden Observatory, Leiden University, P.O. Box 9513, 2300RA Leiden, The Netherlands; abdullah@strw.leidenuniv.nl
[2] Faculty of Aerospace Engineering, Delft University of Technology, Kluyverweg 1, 2629 HS Delft, The Netherlands
[3] Research School of Astronomy and Astrophysics, Australian National University, Mount Stromlo Observatory Cotter Road, Weston Creek, ACT 2611, Australia
[4] Department of Astronomy, University of Maryland, College Park, MD 20740, USA
[5] Department of Astronomy, University of Massachusetts, Amherst, MA 01003, USA
[6] Department of Astronomy, The Ohio State University, 4051 McPherson Laboratory, 140 West 18th Avenue, Columbus, OH 43210, USA
[7] Department of Physics and Astronomy, University College London, Gower Street, London WC1E 6BT, UK
[8] Universiteit Gent, Krijgslaan 281 S9, B-9000 Gent, Belgium
[9] Institute of Astronomy, University of Cambridge, Madingley Road, Cambridge, CB3 0HA, UK
[10] University of San Diego, 5998 Alcala Park, San Diego, CA 92110, USA
[11] Spitzer Science Center, California Institute of Technology, MC 314-6, Pasadena, CA 91125, USA
[12] Department of Physics and Astronomy, University of Wyoming, Laramie, WY 82071, USA
[13] European Southern Observatory, Karl-Schwarzschild-Straße 2, D-85748 Garching, Germany
[14] Department of Astronomy, University of Maryland, College Park, MD 20742, USA
[15] Max-Planck-Institut für extraterrestrische Physik, Giessenbachstraße, D-85748 Garching, Germany
[16] INAF-Osservatorio Astrofisico di Arcetri, Largo E. Fermi 5, I-50125 Firenze, Italy
[17] Department of Physics and Astronomy, University of Toledo, 2801 West Bancroft Street, Toledo, OH 43606, USA
Received 2016 July 8; revised 2017 April 3; accepted 2017 April 24; published 2017 June 6

Abstract

With its relatively low ionization potential, C^+ can be found throughout the interstellar medium (ISM) and provides one of the main cooling channels of the ISM via the [C II] 157 μm emission. While the strength of the [C II] line correlates with the star formation rate, the contributions of the various gas phases to the [C II] emission on galactic scales are not well established. In this study we establish an empirical multi-component model of the ISM, including dense H II regions, dense photon dissociation regions (PDRs), the warm ionized medium (WIM), low density and G_0 surfaces of molecular clouds (SfMCs), and the cold neutral medium (CNM). We test our model on ten luminous regions within the two nearby galaxies NGC 3184 and NGC 628 on angular scales of 500–600 pc. Both galaxies are part of the *Herschel* key program KINGFISH, and are complemented by a large set of ancillary ground- and space-based data. The five modeled phases together reproduce the observed [C II] emission quite well, overpredicting the total flux slightly (about 45%) averaged over all regions. We find that dense PDRs are the dominating component, contributing 68% of the [C II] flux on average, followed by the WIM and the SfMCs, with mean contributions of about half of the contribution from dense PDRs, each. CNM and dense H II regions are only minor contributors with less than 5% each. These estimates are averaged over the selected regions, but the relative contributions of the various phases to the [C II] flux vary significantly between these regions.

Key words: galaxies: ISM

1. Introduction

1.1. The [C II] Line

The [C II] 157 μm is a fine-structure line that arises from the $^2P^0_{3/2} \rightarrow {}^2P^0_{1/2}$ transition of singly ionized carbon, C^+. With an ionization potential of only 11.26 $\sim$ eV, C^+ is found throughout the interstellar medium (ISM). [C II] emission provides one of the main cooling channels in the ISM. With a relative line luminosity of typically $L_{[C\,II]}/L_{FIR} \sim 0.1\%$–$1\%$, it is often the strongest line in the far-infrared (FIR) wavelength regime (Crawford et al. 1985; Stacey et al. 1985, 1991; Wright et al. 1991; Malhotra et al. 2001; Brauher et al. 2008). Observations and theoretical modeling both have indicated that [C II] is the dominant cooling channel in the cold neutral medium (CNM) (Wolfire et al. 2003), and together with [O I], in dense photon dissociation regions (PDRs) associated with regions of massive star formation (Tielens & Hollenbach 1985; Madden et al. 1997; Mizutani et al. 2004; Kaufman et al. 2006).

Previous studies have demonstrated that the strength of [C II] emission correlates well with other star formation tracers (Boselli et al. 2002; de Looze et al. 2011; De Looze et al. 2014; Pineda et al. 2014; Sargsyan et al. 2014; Herrera-Camus et al. 2015), although this relation breaks under certain gas condition. As PDRs are commonly associated with H II regions, in which massive star formation occurred, it is not surprising that [C II] correlates with the star formation rate (SFR). Unlike optical lines such as Hα, [C II] is much less susceptible to dust extinction and has therefore been used as the SFR diagnostic of choice, in particular in luminous star-forming systems (Stacey et al. 1991; Pierini et al. 1999; Boselli et al. 2002). The relation between SFR and [C II] started to be heavily studied with the advent of new sensitive detectors on the Kuiper Airborne Observatory (KAO), the *Infrared Space Observatory* (*ISO*),

the Cosmic Background Explorer (COBE), and balloon observations, and has become a common tool with the advent of the *Herschel Space Telescope* (Stacey et al. 2010; Sargsyan et al. 2012, 2014; Herrera-Camus et al. 2015).

Using [C II] to measure the SFR in galaxies is still problematic. In the extreme case, luminous infrared galaxies (LIRGs) and ultraluminous infrared galaxies (ULIRGs) suffer the so-called "[C II] deficit" problem where the ratio of [C II] to $L_{\rm FIR}$ decreases with increasing ratio of 60/100 micron (FIR color) (Luhman et al. 1998, 2003; Malhotra et al. 2001; Sargsyan et al. 2012; Díaz-Santos et al. 2013; De Looze et al. 2014; Herrera-Camus et al. 2015). An increase in the 60/100 μm ratio indicates warmer dust and more intense radiation fields. The same [C II] deficit is seen also in our Galactic Center (Nakagawa et al. 1995), local galaxies (Malhotra et al. 2001; Beirão et al. 2012; Croxall et al. 2012), and in a large sample of subgalactic regions of KINGFISH data (Smith et al. 2017). The [C II] deficit suggests that caution must be taken if we wish to use [C II] as an SFR tracer in different ISM conditions. All of these studies point out that examining the gas heating-cooling processes under different conditions is necessary to better understand the SFR probed by [C II].

Several observational studies have shown that [C II] can arise from phases of the ISM different than the dense PDRs and SfMCs, these include H II regions (Carral et al. 1994), the diffuse cold or warm neutral medium (CNM/WNM) (Bock et al. 1993; Ingalls et al. 2002), and the warm ionized medium (WIM) (Heiles 1994). The WIM is pervasive throughout the ISM and can give rise to both [N II] and [C II] emission (Heiles 1994). Given its ionization and critical density (Table 2), the [N II] 205 line traces the WIM, the ionized ISM phase with low electron density. In particular, Bennett et al. (1994) found that the [C II] intensity correlates well with the intensity of the [N II] 205 as measured in the large beam size (7°) of COBE. Goldsmith et al. (2015) show based on GOTC+ data and *Herschel* [N II] 205 that [C II] emission and [N II] 205 are correlated morphologically. On the other hand, Crawford et al. (1985) concluded from KAO observations that on a galactic scale, [C II] emission arises from molecular clouds exposed to UV fields with 10–300 times the local interstellar radiation field. The recent study of GOTC+ (Pineda et al. 2013) revealed that [C II] in the Galactic plane is produced by dense photon-dominated regions (≃47%), with smaller contributions from CO-dark H_2 gas (≃28%), cold atomic gas (≃21%), and ionized gas (≃4%).

In this paper we examine the [C II] emission from selected regions within the galaxies NGC 3184 and NGC 628 (see Section 1.3). The aim of this work is to quantify the relative contributions to [C II] from different ISM phases within these regions. We define five components ("phases") of the ISM as follows: (1) dense H II regions, (2) low-density WIM, (3) dense PDRs, (4) low $n_{\rm H}$ and low G_0 surface of molecular clouds (SfMCs), and (5) the diffuse neutral medium (see Section 3.2 and Table 1 for more details). We use the observed emission lines, listed in Table 2, to probe the physical conditions of these phases. For a more detailed discussion on the multiphase ISM we refer the reader to Section 3.1.

This paper is organized as follows: in Section 2 we describe the observations and main data reduction steps. In Section 3 we characterize the multiple phases of the ISM and their contributions to the [C II] emission. We describe our method in Section 4 and discuss the results in Section 5. We finish with a Summary and Outlook in Section 6.

1.2. Estimating the Energy Budget

In this paper we assume that the heating energy of the gas originates from the photons of massive young stars. For simplicity we do not take other sources of mechanical heating into account, i.e., turbulence, which can also be important to the physics and chemistry of the ISM phases, as has been seen in the high-latitude Galatic diffuse clouds (Ingalls et al. 2002). The regions that we inspect are mainly active star-forming regions and do not represent the diffuse cold ISM. Hence the contribution from mechanical heating is considered to be small. We infer the ionizing energy from the extinction-corrected Hα flux, which traces photons with $h\nu \geqslant 13.6$ eV that ionize surrounding hydrogen gas, creating H II regions. Some fraction of these photons leaks into the diffuse ISM, possibly because of the clumpy structure of H II regions. These leaked photons create a low-density ionized phase called the WIM. We find that the Hα luminosities of our studied regions with H II region size of 30–170 pc well exceed those of the Orion nebula or M17, but are an order of magnitude lower than 30 Dor in the Large Magellanic Cloud (LMC) (Kennicutt et al. 1989; Doran et al. 2013).

Photons with energy lower than the ionization energy of neutral hydrogen (13.6 eV) are able to escape the H II region and become the energy source for adjacent dense PDRs, for the surfaces of molecular clouds (SfMCs), and for the diffuse neutral medium. To calculate the incident radiation field, we convert the number of ionizing photons (NLyC) to $L_{\rm UV}$ defined as stellar luminosity between 6 and 13.6 eV using Starburst99 (SB99; Leitherer et al. 1999), assuming a continuous SFR over 10 Myr following the classical Salpeter initial mass function (Salpeter 1955).

The incident radiation field or G_0 can in principle also be calculated from the infrared radiation. This can be done by assuming that the $L_{\rm UV}$ is fully absorbed by dust and re-emitted in the FIR. The incident radiation field G_0 can also be determined by fitting a dust model to the infrared spectral energy distribution (SED) to determine the heating radiation fields. We use the dust model of Draine & Li (2007), in particular the fitting described in Aniano et al. (2012), which provides an estimate of the minimum value of the Mathis radiation field. Mathis et al. (1983) evaluated the background radiation field from 5.04 to 13.6 eV to be 1.14 in terms of Habing fields (Habing 1968). Habing fields are defined as background radiation fields between 6–13.6 eV and have a value of 1.2×10^{-4} erg cm^{-2} s^{-1} sr^{-1} (Draine 2010; Tielens 2010). The dust model of Draine & Li (2007) and Aniano et al. (2012) adopts a two-component model for the dust emission of the region. One component is the fraction ($f_{\rm PDR}$) of the total infrared (TIR) emission that originates in dense PDRs due to the illumination by an enhanced radiation field, commensurate to the stellar luminosity and size of the H II region (G_0 from $L_{\rm UV}$). This component accounts for the illumination of dense PDRs by regions of massive star formation. The second component is the fraction $(1 - f_{\rm PDR})$, which is attributed to the low UV field. It corresponds to the CNM and the SfMCs. For our analysis we adopt the fitted values for our two target galaxies of $f_{\rm PDR}$, and the average UV field, G_0 dust, from the analysis of the dust SED by Aniano et al. (2012). These values are also listed in Table 5.

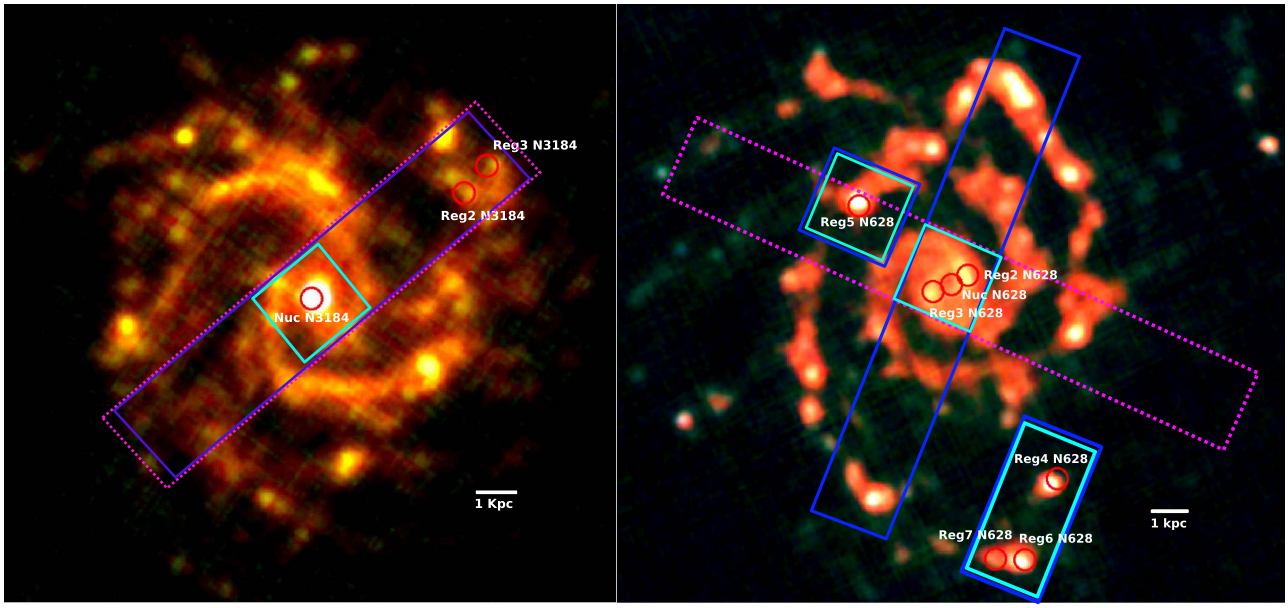

Figure 1. False-color images of NGC 3184 (left) and NGC 628 (right) at 70 μm (blue), 100 μm (green), and 160 μm (red) as observed with PACS. The dotted pink rectangle shows the regions covered by the *Spitzer* IRS LL-module, while the dark blue solid rectangle shows the area for which PACS spectroscopy in [C II], [O I], and [O III] is available. The cyan rectangle shows the observed strip of [N II] 122. The regions selected for this study are indicated by red circles and listed in Table 4. Each circle refers to a flux extraction aperture of 12″ in diameter, which corresponds to physical sizes of 600 and 500 pc for NGC 3184 and NGC 628, respectively.

1.3. NGC 3184 and NGC 628

The improvements in spatial resolution and sensitivity of the new generation of FIR and submillimeter observatories, *Herschel* (Pilbratt et al. 2010) and ALMA (Hills & Beasley 2008), offer the opportunity to study heating and cooling processes in the ISM of galaxies in great detail. In this paper we use the instruments on board *Herschel* and combine them with diagnostics at shorter wavelengths that were previously taken with the *Spitzer Space Telescope* or from the ground. For this case study we have selected a total of ten regions in the two nearby galaxies, NGC 3184 and NGC 628. These galaxies have been selected on the basis of their existing multiwavelength data sets. Both galaxies are members of the *Herschel* open time key program KINGFISH, which stands for Key Insights into Nearby Galaxies: Far-Infrared Survey with *Herschel* (Kennicutt et al. 2011), providing both FIR dust continuum observations and the vital FIR spectroscopy measuring the [C II] and other fine-structure lines listed in Table 4.

Within each galaxy, these regions sample the nuclei and the spiral arms, and are bright in the FIR lines of [O I]63 μm, [N II] 122 μm, [O III]88 μm, and [C II]157 μm. The ten regions have been selected based on their high signal-to-noise ratio (S/N) in the optical maps of PPAK Integral Field Spectroscopy Nearby Galaxies Survey (PINGS) (Rosales-Ortega et al. 2010; Sánchez et al. 2011). In addition to the PINGS data, a wealth of ancillary data at other wavelengths exists: FUV and NUV by *GALEX* (Martin et al. 2005), optical BVRI bands at the Kitt Peak National Observatory (KPNO) as part of the *Spitzer* Infrared Nearby Galaxies Survey (SINGS) program, and NIR-MIR from SINGS (Kennicutt et al. 2003).

We need to emphasize that while modern optical and infrared observatories enable spatially resolved studies of galaxies beyond the Local Group, their *spectroscopic* sensitivity is still limited to the more luminous regions within the galaxies. By necessity, this introduces a selection bias toward regions of massive star formation since the "colder" non-star-forming regions provide insufficient S/N for detailed spectroscopic studies (see also Section 4.6). This general limitation also applies to our study of NGC 3184 and NGC 628 (Figure 1).

Both galaxies are shown in Figure 1. Their dust properties (dust-to-gas ratio, polycyclic araomatic hydrocarbon, PAH, mass fractions relative to the total dust mass) and UV-radio SEDs have already been studied within the SINGS project (Dale et al. 2007; Draine & Li 2007). NGC 3184 is a SAB(rs) cd type galaxy located at the distance of 11.6 Mpc, while NGC 628 is an SA(s)c type galaxy located at 7.2 Mpc (Kennicutt et al. 2003). At this distance, an aperture size of 12″ corresponds to a physical size of 500–600 pc. On this scale it is very likely to have multiple H II regions and dense PDRs within one beam. For comparison, 30 Dor in the LMC stellar cluster has a half-light radius of 70 pc (Shields 1990). The two galaxies, based on their averaged stellar formation rate, are categorized as normal galaxies (Kennicutt et al. 2003, 2011). We select regions with ongoing star formation (H II regions), measured from their Hα flux (also see Figure 2). We list the general properties of the two galaxies in Table 3.

2. Observations and Data Reduction

The *Herschel* KINGFISH survey is an imaging and spectroscopic survey of 61 nearby galaxies that were chosen to cover a large range of galactic properties. It is descended from the SINGS program (Kennicutt et al. 2003), and one of its main aims is the study of the heating and cooling processes in the ISM within spatially resolved galaxies. Here we describe the KINGFISH photometry and spectroscopy, and give a summary of the ancillary data used in this analysis.

2.1. KINGFISH Photometry

The KINGFISH photometry includes data from both the Photodetector Array Camera and Spectrometer (PACS) (Poglitsch et al. 2010) and the Spectral and Photometric

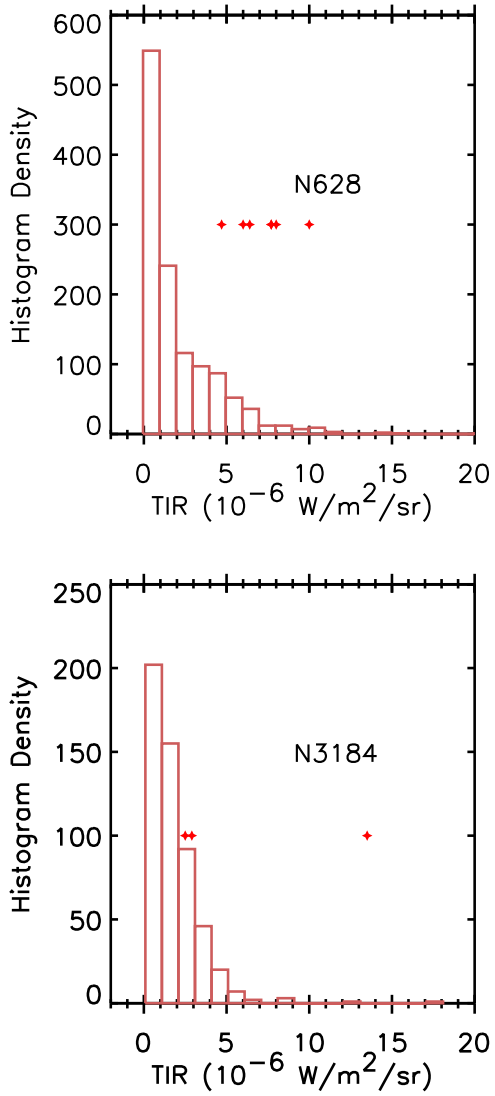

Figure 2. Histogram of the total infrared (TIR) emission per telescope beam (at 160 μm) across the galactic disk for both NGC 628 (top) and NGC 3184 (bottom). The TIR values of the selected regions are indicated by red crosses.

Imaging Receiver (SPIRE) (Griffin et al. 2010). However, we use only the three PACS broadband filters, centered on 70, 100, and 160 μm, for our analysis because of the low spatial resolution of the SPIRE data. The KINGFISH photometric observations were designed to reach a sensitivity of 1σ per pixel ($\sim$1 MJy sr^{-1}) at 160 μm at the optical radius of R_{25} (Kennicutt et al. 2011). The PACS images were taken in scanning mode with a scanning speed of 20″ s^{-1}. Initial data reduction was performed with the Scanamorphos package (Roussel 2013). The reader is referred to the papers by Kennicutt et al. (2011) and Dale et al. (2012) for more details of the data reduction steps performed on the KINGFISH galaxies.

We used the library of convolution kernels, provided by Aniano et al. (2011), to match the different resolutions at the various wavelengths. We convolved all our broadband PACS images to match the resolution of the PACS 160 μm map, which corresponds to approximately 12″. We used this angular size to define our regions of interest (described in Section 3.1), and extract all our photometric fluxes in apertures of 12″ diameter centered on our regions (see Table 4).

2.2. KINGFISH Spectroscopy

PACS spectroscopy provides access to some of the most important diagnostic and cooling lines in the FIR, most notably [C II]157 μm, [O I]63 μm, [O III]88 μm, and [N II]122 μm. All of the three regions we select in NGC 3184, and four regions in NGC 628 have IRS observations from SINGS. They are covered by PACS spectroscopic observations, which gives us access to some of the most important diagnostic and cooling lines such as [C II]157 μm, [O I]63 μm, and [O III]88 μm dotted, pink rectangle in (see Figure 1). Only the nuclei of NGC 3184 and NGC 628 were observed in the [N II]122 (cyan square in Figure 1) with the additional observation of [N II]205 for NGC 628.

The regions of NGC 3184 that match the IRS strip observed by SINGS have also been observed with PACS in the [C II]157, [O I]63, and [O III]88 lines (dotted pink rectangle in Figure 1), while for NGC 628 the IRS strip is orthogonal with respect to the PACS observational strip (see Figure 1). The nuclei of NGC 3184 and NGC 628 were also observed in the [N II] 122 line (cyan square in Figure 1). Additional observations in the [N II] 122 and [N II] 205 lines have been taken in NGC 628. Unchopped-line scans were performed on both galaxies. To overcome the effect of undersampling and to minimize the gap between pointings, a dither pattern of 23.″5 × 23.″5 was imposed (Kennicutt et al. 2011). For single-pointing maps, i.e., in the [N II]122 line, a 2 × 2 subpixel dither pattern of 4.″5 × 4.″5 was performed to overcome this problem. The *Herschel* Interactive Processing Environment pipeline version 8.0 has been used to reduce the PACS spectroscopy maps (Ott 2010), which have calibration uncertainties of 15%. The line map of each emission was created after removing the line continuum by third-order polynomial fitting. The line profile was then fitted with a Gaussian function. When the fit failed to converge, direct integration was performed instead. The reader is referred to the paper by Croxall et al. (2012, 2013) for more details of the spectroscopic data reduction steps performed on the KINGFISH galaxies. The line uncertainty is calculated from the calibration and line fitting process.

On average, we reached a surface brightness sensitivity of 10^{-10}–10^{-9} W m^{-2} sr^{-1} for all PACS spectroscopy lines. We extracted the line fluxes inside photometric apertures with 12″ diameter and present the resulting surface brightnesses in Table 4. For each line, we present the flux derived from the maps at their original spatial resolution. When comparing lines and deriving line ratios, we convolve to a common spatial resolution.

2.3. Ancillary Data

2.3.1. Spitzer Photometry

We obtained the *Spitzer*-IRAC (Fazio et al. 2004; Werner et al. 2004) (3.6–8.0 μm) and MIPS 24 μm maps from the SINGS database (Kennicutt et al. 2003; Dale et al. 2007). We convolved all ancillary images to the resolution of PACS 160 μm using the convolution kernels of Aniano et al. (2011).

2.3.2. IRS Spectroscopy

We used the *Spitzer* IRS (Houck et al. 2004) Long-Low (LL) data from 14 to 40 μm for our analysis. The observed IRS LL strips are overlaid in Figure 1. We extracted the LL flux inside the 12″ aperture using CUBISM (Smith et al. 2007a). We combined the LL1 and LL2 spectral segments after scaling the

continuum level of LL2 to match that of LL1. We then fitted the data cube using PAHFIT (Smith et al. 2007b) to obtain line maps of [Ne III]15.5 μm, H_2 (S1) 17.0 μm, [S III]18.7 μm, H_2(S0) 28.2 μm, [S III]33.4 μm, and [Si II]34.8 μm. We extracted the line fluxes in 12″ apertures and list them in Table 4. We derive the uncertainty on the IRS flux based on the uncertainty of PAHFIT fitting procedure (Smith et al. 2007b).

2.3.3. CO ($J = 2 \rightarrow 1$) and H I Data

We used the CO ($J = 2 \rightarrow 1$) data from the HERA CO-Line Extragalactic Survey (HERACLES) program (Leroy et al. 2009). The emission line map has a beam resolution of 13″ (Leroy et al. 2009). The H I data have been taken from The H I Nearby Galaxy Survey (THINGS) (Walter et al. 2008). The typical beam size for the H I map is 6.″5–7.″5 for both galaxies. We did not convolve the H I maps to a lower resolution. The uncertainty is calculated from rms scatter and the systematic uncertainty (Leroy et al. 2009).

2.3.4. PINGS Optical Spectroscopy

For optical spectroscopy, we used data from the PPAK Integral Field Spectrograph (Kelz et al. 2006; Rosales-Ortega et al. 2010). The data on NGC 628 have been made publicly available by the PINGS program (Rosales-Ortega et al. 2010; Sánchez et al. 2011). The data on NGC 3184, which had already been taken but not yet published, have been been kindly provided by F. Rosales-Ortega.

The PPAK integral field unit (IFU) has dimensions of 74″ × 65″, using fiber bundles with diameters of 2.″7 each. Approximately 16 pointings with the IFU were obtained on NGC 3184, covering a large part of the galaxy. Since dithering was not performed on NGC 3184, we are missing the flux that falls in the gaps between the individual fibers. On NGC 628, an area of 34 arcmin^2 was observed, and dithering was performed for some of the pointings. For more details on the observations and data reduction, we refer the reader to Rosales-Ortega et al. (2010).

We matched the coordinates of the PINGS maps to the coordinates of the SINGS Hα maps. The Hα images were obtained with the KPNO and CTIO telescopes using a set of narrowband filters centered on Hα. Comparison between the PINGS and the stellar continuum-subtracted Hα SINGS line intensity revealed a discrepancy in the fluxes, with PINGS Hα fluxes being about 4–7 times higher. Additionally, we compared the Hα PINGS flux with the Hα flux inside a 2.″5 × 2.″5 aperture from Moustakas et al. (2010). The result is similar, the PINGS Hα fluxes are significantly higher, while the Hα fluxes from Moustakas et al. (2010) and SINGS agree within 20%. This discrepancy is most likely due to the difficulty in absolute flux calibration of the sparsely sampled fibers in the PINGS data. The PINGS survey focuses on line ratios, not on absolute fluxes, and we similarly only used line ratios. The relative flux calibration is accurate to within 5% for the whole mosaic (private communication with F. F. Rosales-Ortega). To obtain the absolute flux calibration, we scaled all optical lines in the PINGS spectra such that the Hα fluxes matches those determined from the narrowband imaging SINGS data. As we uniformly scaled all lines, leaving the line ratios unchanged, this does not affect the ionized gas modeling of the optical lines in the later sections. However, the scaling affects the determination of the ionizing luminosity (NLyC), which in turn affects our predicted [C II] luminositites arising from H II regions (Section 4.1). The line intensity uncertainty was derived from the calibration and reduction step, which is ∼20% in the case of NGC 3184 and 30% for NGC 628 (F. F. Rosales-Ortega 2017, private communication).

We used the extinction law from Fitzpatrick (1999) to correct the optical emission for dust extinction. We assumed "case B" recombination with T_e = 10,000 K, and an intrinsic ratio of Hα over Hβ of 2.86 (Osterbrock & Ferland 2006). We calculated the color excess for each of the regions measuring the intensity-weighted averaged A_V inside the 12″ aperture. We found that A_V ranges from 0.4 to 1.2 mag. The extinction-corrected surface brightnesses inside the 12″ apertures are presented in Table 4. The MAPPINGS models were compared to these extinction-corrected line fluxes.

3. The Five Modeled Phases of the ISM

3.1. A Multiphase ISM

In the following section we give a brief overview of the literature on the topic of the multiphase ISM. We emphasize that these studies investigated different objects with different physical sizes. Most of these studies focused on small scales within well-resolved (nearby) objects. Some discrepancies in their results are therefore to be expected.

Madden et al. (1993) were among the first to suggest that the [C II] originates from a multiphase ISM (WIM, dense PDR, and CNM). Since then, many attempts have been made to disentangle the contributions of the multiple ISM phases (H II regions, CNM, WIM, dense PDRs (such as the Orion bar), or from the surface of molecular clouds (SfMCs) to the observed [C II] emission (Mookerjea et al. 2011; Beirão et al. 2012; Cormier et al. 2012; Croxall et al. 2012; Lebouteiller et al. 2012; Madden et al. 2013; Pineda et al. 2013). In this section, we describe the model used in the analysis. We find that the general picture is confusing and different studies come to sometimes different conclusions on the relative importance of the various components.

Heiles (1994) and Velusamy et al. (2012) advocated the importance of diffuse ionized gas (the WIM) to the [C II] from the Milky Way. Bennett et al. (1994) showed from COBE observations of Milky Way that the [C II] intensity correlates with the [N II]205 intensity. In the Milky Way, [N II]205 is expected to arise predominantly from extended low-density H II regions associated with the H II envelopes of spiral arms with $n_{cr} \simeq$ 40–100 cm^{-3} (Heiles 1994), similar to what Oberst et al. (2006) found for the Carina Nebula. Likewise, while the inferred densities are much higher (n_e = 100–400 cm^{-3}) than WIM densities, Carral et al. (1994) found that 30% of [C II] in NGC 253 comes from H II regions. A very different picture was developed by Vastel et al. (2001) and Mizutani et al. (2004), in which [C II] mainly arises from dense PDRs, following the theoretical work of Tielens & Hollenbach (1985) and Kaufman et al. (2006). Indeed, a number of observations demonstrated that [C II] originates from the dense PDR interfaces that separate ionized gas from the surrounding molecular clouds (Crawford et al. 1985; Shibai et al. 1991; Stacey et al. 1993; Matsuhara et al. 1997; Orr et al. 2014). Finally, other studies (Bock et al. 1993; Wolfire et al. 1995; Ingalls et al. 2002) have suggested that [C II] on a galactic scale arises from cold diffuse clouds (the CNM).

Table 1
ISM Components

Characteristic	H II Region	WIM	Dense PDR	SfMC	CNM
Location	surrounding OB stars	pervasive in ISM	adjacent H II region	surface of MCs	pervasive in ISM
Ionization state	highly ionized	ionized	neutral	neutral	neutral
Typical T_{gas} (K)	7000–10^4	$\sim 10^4$	$\sim$300 (Orion PDR)	100–300	$\sim$80
Typical n_e or n_H (cm^{-3})	100–10^4	0.1–10	$\sim 10^4$–10^5	10^2–10^3	$\sim$50
Typical P/k (K cm^{-3})	$8 \cdot 10^6$–10^7	80–8000	p equil.H II regions[a]	8000–10000	1000–10000
Heating mechanism	photoelectrics, photoionization	photoionization	photoelectric, FUV pumping	photoelectric	photoelectric

Notes. The five phases are chosen based on the findings of previous studies (see Section 3.1). The given numbers in the table are compiled from various authors: Osterbrock & Ferland (2006), Draine (2010), Tielens (2010), and Wolfire et al. (1995).
[a] Pressure equilibrium with the H II region component. For more details on P/k see Sections 4.4 and 4.5.

Several *Herschel* studies took into account the complexity of the ISM and simultaneously modeled the [C II] from multiple phases. Beirão et al. (2012) and Croxall et al. (2012) demonstrated that about 3%–50% of the [C II] arises from ionized gas, with no distinction between that arising from H II regions and WIM-like gas. A similar percentage has also been found by Goldsmith et al. (2015) from Galactic Observations of Terahertz C+ (GOTC+) in a recent study of the Milky Way: about 30%–50% of [C II] arises from ionized gas. A different picture, however, was shown by Cormier et al. (2012) for low-metallicity dwarf galaxy of Haro 11, wihere [C II] comes to 40% from the ionized diffuse medium and 10% comes from PDRs. Cormier et al. (2012) filled up the missing [C II] by introducing diffuse PDR components into their model. Pineda et al. (2013) showed from the GOTC+ survey that 47% of [C II] in the Galactic plane comes from PDRs with gas densities $\sim 10^3$–10^4 cm^{-3} and G_0 in the range from 1 to 30, while the rest arises from CO-dark H_2 gas (28%), CNM, and WNM (21%), and small amounts of ionized gas (4%).

Kapala et al. (2015) analyzed regions in M31 with physical sizes comparable to our regions, namely 700 pc apertures with 50 pc resolution. They found for M31 that from 20% to 90% of the [C II] comes from outside star-forming regions. The rest originates in the ISM and is related to star-forming regions (H II and PDRs).

A detailed modeling scheme is needed to determine the contribution of the different ISM components to the [C II] emission and to understand how relative contributions change with the physical conditions in the ISM. A better understanding on the overall picture of the gas heating and cooling can be used to calibrate the use of [C II] to probe the star formation process. In this section we define a set of ISM phases (Section 3.2). We then model the [C II] emission from these different ISM phases independently from each other for two target galaxies (Section 4).

3.2. Definition of the Five Phases

Following the literature, we define the following five ISM phases and summarize their characteristics in Table 1:

1. *Dense H II regions* are the ionized gas surrounding the young stellar clusters with typical density ranges from 100 to 10^4 cm^{-3} and a gas temperature of $\sim$8000 K (Osterbrock & Ferland 2006).
2. *WIM* is the extended diffuse ionized phase. Some of the photons from the stellar cluster can leak and travel to large distance and ionize less dense gas, which creates this ISM phase. The typical densities are in the order of 0.1 cm^{-3} (Haffner et al. 2009), as obtained from dispersion measures.
3. *Dense PDRs* are largely neutral, associated with (or surrounding) H II regions, and are characterized by high densities (n_H) and high incident radiation fields (G_0). The Orion bar provides a good example.
4. *SfMCs*. SfMCs are PDRs characterized by low G_0 and low n_H. They represent extended regions of massive star formation where molecular clouds are exposed to the local average interstellar radiation field. The SfMCs are essentially PDRs (Hollenbach & Tielens 1997) characterized by low densities and the average interstellar radiation field.
5. *The diffuse neutral medium* consists of two components: the CNM ($T \sim$ 40–100 K) and the WNM (5000–10,000 K) (Heiles & Troland 2003). We do not model the WNM here because we infer from models for the emission of the phases of the ISM (Wolfire et al. 1995) that its contribution per hydrogen is only 0.1 on average relative to CNM gas and it does not have a distinct tracer.

We make use of CO($J = 2 \rightarrow 1$) as a molecular cloud tracer, H I as a neutral medium tracer, and optical emission lines as tracers of H II regions. The WIM contribution is not constrained by any specific observation. These diagnostics are then used to constrain the models and predict the [C II] emission. For a more detailed description of the methods used, we refer the reader to Figure 3. In general, we do not take into account the specific geometry that the ISM phases may have. In order to calculate the gas properties (G_0 and n_H) for the dense PDRs from the gas properties of the H II regions, we have to assume a spherical geometry. For other ISM phases, however, we assume no specific geometry with respect to the central stellar populations. The other three ISM phases are expected to extend beyond the physical size covered by one beam; this assumption implies that there is no connection between the dense PDR and the surface of molecular clouds in general. In our analysis, we attribute all the H I to the diffuse ISM. This should be seen as an upper limit as some of the H I may arise from the photodissociated surface of molecular clouds (Heiner et al. 2011, 2013).

3.3. Locations and Morphologies of the Regions

At the spatial resolution of these two galaxies, we expect multiple ISM components to overlap in the beam. These components of H II regions and PDRs typically appear as

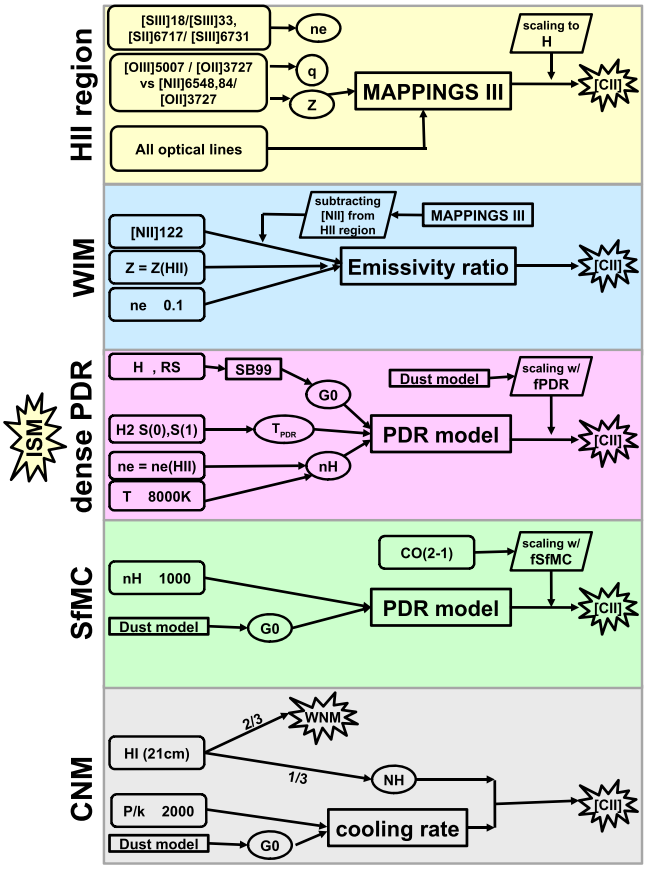

Figure 3. Overview of how the [C II] flux contributions were derived for each of the five modeled ISM phases.

compact unresolved objects, while the CNM and WIM are more diffuse components that may extend well beyond the region corresponding to one beam size. Furthermore, they are seen at low inclination, which minimizes dust obscuration and line-of-sight confusion. We select three regions in NGC 3184 and seven regions in NGC 628. The ten regions are selected based on the availability of the data. Of the ten selected regions, two are located in the nucleus i.e., at the center of galaxies, while the other eight are located in the spiral arms of the galaxies (see Figure 1). The center of each aperture is selected by the peak brightness of the Hα emission. As can be seen in Figure 1, there is significant emission outside the photometric aperture. We cannot tell whether this emission is physically connected to the H II regions. However, we estimated the error on the fluxes, mostly [C II], from the centering of the aperture for some cases (like for Reg5 NGC 628, where a clear peak is evident). In these cases the errors in the extracted flux can be up to 20%.

We compare the [C II] emission against several other phase tracers such as Hα, [N II] 122, CO ($J = 2 \rightarrow 1$), and H I in Figure 4. The [C II] morphology in general can be divided into two categories: the first category is where we see [C II] emission associated with the region (see Figure 4). This applies to regions Nuc. N3184, Reg2 N628, Reg4 N628, Reg5 N628, and Reg6 N628. The second category is where the [C II] emission is rather weak and diffuse, as shown by Reg2 N3184, Reg3 N3184, Nuc. N628, and Reg7 N628. In four regions, the Hα emission coincides with the [C II] emission. These regions are Nuc N3184, Reg4 N628, Reg5 N628, and Reg6 N628. We find three regions where the [C II] emission coincides with the CO($J = 2 \rightarrow 1$) emission (Nuc N3184, Reg2 N628, and Reg5 N628). However, only three regions show a correlation with [N II] 122, namely Nuc. N3184, Reg4 N628, and Reg5 N628. In most regions we find that the 8 μm emission, which comes from stochastic heating process of PAHs and small-grain continuum emission (Tielens et al. 1999), correlates well with the [C II] emission. This is not surprising as the two are related through the photoelectric heating process (Helou et al. 2001). We find little or no correlation between [C II] emission and H I. Pineda et al. (2013) showed that the H I distribution in our Galaxy is smoother than the [C II] emission, given that the beam of H I is smaller than the [C II] beam. We stress that in our analysis of individual regions, correlation or non-correlation in morphology does not determine our estimate of the contribution of a specific phase to the [C II] emission in that region.

4. Analysis of the Gas Conditions and the Modeled [C II] Emission

In this section we use a wide range of spectroscopic data from Table 4 to derive for each of the ten distinct regions (Section 3.3) within NGC 3184 and NGC 628 the main physical properties of the individual ISM phases, such as density, strength of the radiation field, and gas temperature. With these physical parameters in hand, we can then model the fractions of the observed [C II] flux coming from the individual ISM phases. The systematic uncertainties of the individual contributions to the [C II] emission are discussed in Section 4.6.

4.1. The H II Region

An H II region is confined by an ionization front. Photons with energies lower than 13.6 eV can easily escape the region, while most of the ionizing photons with energies $E \geqslant 13.6$ eV are absorbed inside the Strömgren radius to ionize hydrogen. The ionized gas cools through cooling lines, which radiate away energy. Most of these cooling lines lie in the optical wavelength range (see Table 2). These lines serve as good diagnostics of the physical conditions in the H II region.

The optical spectra of H II regions are governed by three parameters: (i) the electron density (n_e), (ii) the ratio of photon density to particle density (or ionization parameter, q, as defined in Dopita et al. 2000), and (iii) the metallicity Z. We use an analytical calculation to guide us through the parameter space (see Appendix A.1).

The optical line fluxes guide the initial parameter ranges of MAPPINGS III to model the gas condition of the H II region to compare it to observations. The optical lines used are [O II]3728, [O III]4959, [O III]5007, Hα, [N II]6548, [N II]6584, [S II]6717, [S II]6731, and Hβ. We calculated a set of model spectra for varying n_e and q, while we kept the metallicity fixed. The n_e was set to several values between 1 and 10^4 cm^{-3}, while q was chosen to range between 1×10^6 and 4×10^8. We chose optical lines rather than mid-IR (MIR) lines ([Ne III]15 μm, [S III] 18 μm, and [S III] 33 μm), as the relative uncertainty within the optical set is smaller than the discrepancy between optical set and MIR lines. As a sanity check, we compared two cases of MAPPINGS III modeling. First, we modeled only optical lines, and second, where we modeled all lines including the MIR lines. The second case yields gas conditions with unphysical properties where the

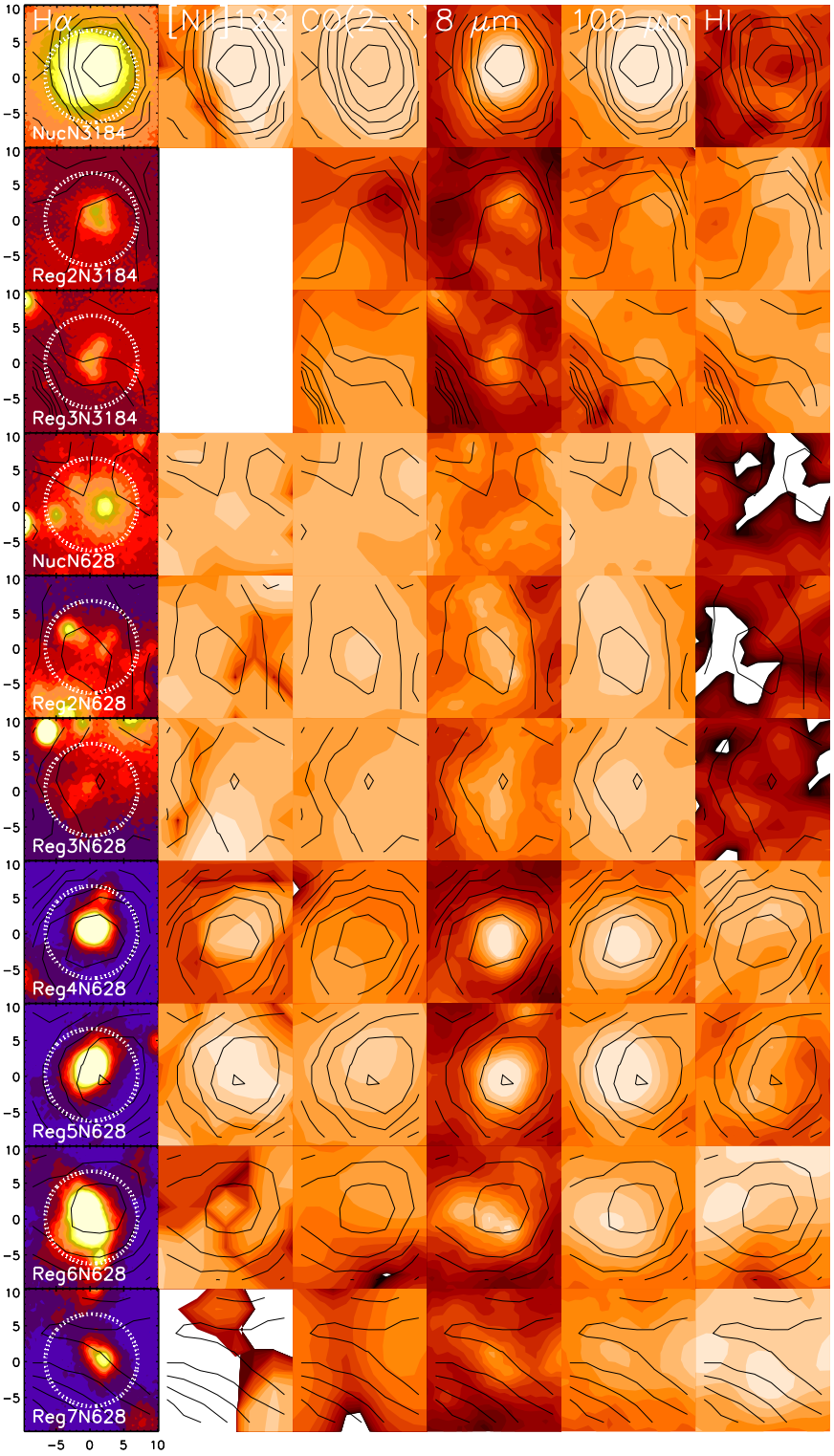

Figure 4. Comparison of the [C II]157 μm contours with other tracers in their original resolution. One arcsecond in this image corresponds to 55 and 42 pc in physical scale for NGC 3184 and NGC 628, respectively. The photometry aperture is marked by the white dotted circle. The angular resolutions of the various maps are as follows: Hα $\sim 1''$ (http://www.noao.edu/kpno/imaging/imaging.html), [N II]122 μm $\sim 10''$ (http://herschel.esac.esa.int/Docs/PACS/html/pacs_om.html), CO ($J = 2 \rightarrow 1$) $\sim$13$''$ (Leroy et al. 2009), IRAC 8 μm $\sim 2''$ (Croxall et al. 2012), 100 μm $\sim 6\farcs9$ (Croxall et al. 2012), H I beam size $6\farcs8 \times 5\farcs6$ for NGC 628 and $5\farcs3 \times 5\farcs1$ for NGC 3184, respectively (Walter et al. 2008). The [C II] contour levels are 5.5×10^{-8}, 3.8×10^{-8}, 2.6×10^{-8}, and 1.8×10^{-8} W m^{-2} sr^{-1}.

ionization parameter is by one order of magnitude lower than the typical H II regions.

We assume a continuous SFR and constant pressure throughout the H II region. Since MAPPINGS III yields the ratio between [C II] and Hβ, the filling factor cancels out. We consider only optical lines that have been detected at S/N $\geqslant 3$, and use a reduced χ^2 minimization to determine the best fit, weighted by the measured uncertainty in the observed flux. The fit result is non-degenerate with n_e varying from 500 to 1000 (see Figure 5), while q varies between 1×10^7–4×10^7.

Table 2
Emission Lines for Analysis

Line	Ionization $P.$ (eV)	$n_{cr.}$ (cm^{-3})	E_{ul} (K)	Tracer
[O II] 3727,3729 Å	13.6	1.3×10^3[e]	3.9×10^4	H II region
H_β 4863 Å	13.6	...	...	H II region
[O III] 4959 Å	35.1	6.9×10^5[e]	2.9×10^4	H II region
[O III] 5007 Å	35.1	6.9×10^5[e]	2.9×10^4	H II region
[N II] 6548 Å	14.5	8.6×10^4[e]	2.2×10^4	H II region
Hα 6564 Å	13.6	...	...	H II region
[N II] 6584 Å	14.5	8.6×10^4[e]	2.2×10^4	H II region
[S II] 6718 Å	10.4	1.3×10^3[e]	2.1×10^4	H II region
[S II] 6731 Å	10.4	3.6×10^3[e]	2.1×10^4	H II region
H_2(0,0) (S1)17.0 μm	...	2×10^4[H]	1.0×10^3	dense PDR
H_2(0,0) (S0) 28.2 μm	...	7×10^2[H]	5.1×10^2	dense PDR
[O I] 63 μm	...	9.7×10^5[H]	2.3×10^2	dense PDR
[O III] 88 μm	35.1	5×10^2[e]	1.62×10^2	H II region
[N II] 122 μm	14.5	2.8×10^2[e]	1.2×10^2	WIM, low-density H II gas
[C II] 157 μm	11.3	6.3×10^0[e], 2.7×10^3 [H]	9.2×10^1	
[N II] 205 μm	14.5	4.5×10^1[e]	7.0×10^1	WIM, low-density H II
CO (2-1)	...	2.4×10^4	16.6	SfMC PDR
H I 21 cm	...	...	...	CNM, WNM

Table 3
Global Properties of NGC 3184 and NGC 628

Properties	NGC 628	NGC 3184
L_{TIR} (3–1100 μm) ($L_\odot$)[a]	8.0×10^9	1.1×10^{10}
L_B ($L_\odot$)[b]	1.9×10^{10}	3.4×10^9
L_{UV}($L_\odot$) (6–13.6 eV)[c]	$\geqslant 1.8 \times 10^{10}$	$\geqslant 3.2 \times 10^9$
H I mass ($M_\odot$)[d]	3.8×10^9	3.1×10^9
M_{dust} ($M_\odot$)[e]	2.9×10^7	4.2×10^7
M_* ($M_\odot$)[f]	3.7×10^9	1.7×10^9
D (Mpc)[g]	7.2	11.6
H_2 ($M_\odot$)[h]	1.2×10^6	2.1×10^7
Global $SFR_{H\alpha + 24}$ ($M_\odot$ yr^{-1})[i]	0.66	0.68
log[O/H]+12[j]	9.02 ± 0.01	9.15 ± 0.01
Gradient of log[O/H]+12 (dex per R_{25})[k]	-0.52 ± 0.04	-0.57 ± 0.04
D_{25} (arcmin)[l]	10.5×9.5	7.4×6.9

Notes.
[a] From Kennicutt et al. (2011).
[b] From Kennicutt et al. (2003).
[c] From converting the NLyC photons number to L_{UV} using SB99.
[d] From Walter et al. (2008).
[e] From Aniano et al. (2012).
[f] From Kennicutt et al. (2011).
[g] From Kennicutt et al. (2011).
[h] From Roussel et al. (2007).
[i] From Kennicutt et al. (2011).
[j] Characteristic value from Moustakas et al. (2010).
[k] From Moustakas et al. (2010), Croxall et al. (2013).
[l] From Kennicutt et al. (2003).

Obviously, the fit result is better constrained by the ionization parameter rather than by the electron density, except for Nuc NGC 628. As expected, the resulting n_e and q values from the MAPPINGS fitting procedure are in good agreement with the preliminary analysis (see Appendix A.1). The electron density derived from the two methods agrees, except for Reg3 NGC 3184, Nuc NGC 628, Reg4 NGC 628, and Reg5 NGC 628, where n_e from the line ratio is by a factor of two higher than in the MAPPINGS III modeling.

Most of the observed line fluxes in the optical and FIR can be reproduced within the 3σ uncertainty of the model (see Figure 6). However, this is not the case for [S III]18, 33 and [Ne III]. According to MAPPINGS III, the MIR [S III]18, 33 and [Ne III] lines should be much brighter with respect to Hβ than what is observed, except for Reg5 N628. We assign this discrepancy to the calibration uncertainty of the set of optical lines with respect to the MIR lines.

If instead we were to base this analysis on the MIR lines, the physical characteristics would change: one order of magnitude lower q and three times higher density. Still, for almost all sources, the contribution of dense H II regions to the observed [C II] emission would be small, in the range of 0.5%–5%. The only exceptions are Nuc N3184 and Reg5 N628, where the analysis of the MIR lines results in densities of 1–10 cm^{-3}, and for such low-density gas the predicted [C II] emission would become important. However, for these two regions, we consider the results from the MIR line analysis with MAPPINGS III as unphysical because ionized gas of such low density could not produce the observed optical line fluxes. The MIR line fluxes may just qualitatively indicate the *presence* of lower density gas. We consider the emission from low-density ionized gas to the observed [C II] emission further in Section 4.2. In summary, we conclude that dense H II regions do not give an important contribution to the observed [C II] line intensity.

In our MAPPINGS calculations we assumed a temperature $T_{e=8000}$ K. We also determined the electron temperatures using CHAOS data (Berg et al. 2015) as a cross-check. Averaging the T_e derived from [N II], [S II], and [O II], we obtained $T_e \sim$ 8000 K for Reg2 NGC 3184 and $T_e \sim$ 7900 K for Reg3 NGC 3184, in excellent agreement with our MAPPINGS parameters.

Based upon the region properties in Table 5, we have calculated the [C II] 157 μm flux densities we expect from H II regions. We derived the absolute [C II] flux by scaling the MAPPINGS output. The scaling factor was derived from the observed Hβ flux. We find from the MAPPINGS model that between 20% and 100% of the observed [N II]122 can be

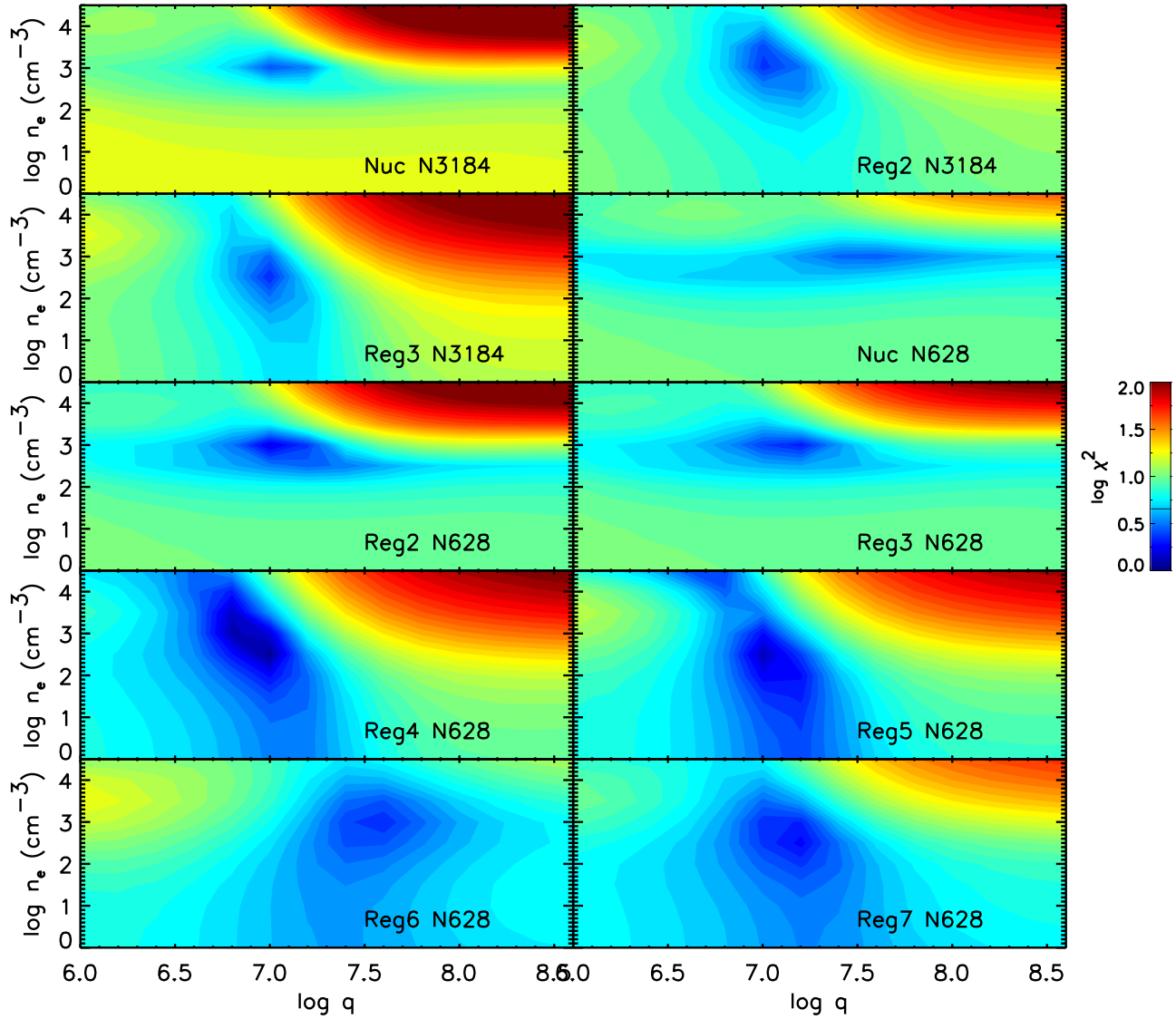

Figure 5. χ^2 fitting from the MAPPINGS model. We fixed the metallicity Z and varied the electron density n_e and ionization parameter q.

provided by the H II regions. We discuss the consequence in Section 4.2.

Reflecting the low critical density of [C II], the high-density H II component adds only 3% to the observed [C II] emission, except for Nuc N3184 and Reg4 N628, where up to 20% are predicted (Table 6). Our findings are in good agreement with a study on NGC 253 by Carral et al. (1994) (with ∼700 pc aperture size) and the Mookerjea et al. (2011) study of star-forming regions in M33 (physical size ∼500 pc). A more recent study of Pineda et al. (2013) of the Milky Way found that 4% of the [C II] rises from ionized gas, while Goldsmith et al. (2015) found that a larger fraction of 30%–50% of [C II] arises from ionized gas. Both studies are performed over physical sizes that are different from our regions.

4.2. WIM

In our study, the WIM is not constrained by any specific observation. Within the available *Herschel* diagnostics, the electron density can be traced by the ratio of the [N II] 205 and [N II] 122 lines (Bennett et al. 1994). Both lines have relatively low critical densities (n_e = 50 and 300 cm^{-3}, respectively) and can be used to estimate the [C II] emission from low-density ionized gas. [N II]122 in particular also arises from H II regions with densities below 300 cm^{-3}. As we have no [N II] 205 flux measurements, we have to rely on [N II] 122 for the [C II] estimation from the WIM. For NGC 628 we have [N II] 122 data for all regions, but for NGC 3184, [N II] 122 data are only available for the nucleus, not for the extra-nuclear regions.

We calculate the emissivity ratio of [C II] over [N II] as a function of electron density.

$$\frac{I_{[\mathrm{C\,II}]}}{I_{[\mathrm{N\,II}]}} = \frac{N_{[\mathrm{C\,II}]\mathrm{u}}}{N_{[\mathrm{N\,II}]\mathrm{u}}} \times \frac{E_{[\mathrm{C\,II}]\mathrm{ul}}}{E_{[\mathrm{N\,II}]\mathrm{ul}}} \times \frac{A_{[\mathrm{C\,II}]\mathrm{ul}}}{A_{[\mathrm{N\,II}]\mathrm{ul}}}. \quad (1)$$

Following Rubin (1984) and Sembach et al. (2000), we assume that the ionic abundance ratios of [C II] over [N II] are equal to their elemental abundance ratio. The upper-level population of [N II], ($N_{[\mathrm{N\,II}]\mathrm{u}}$), is calculated based on the assumption of a three-level system, while the upper-level population of [C II], ($N_{[\mathrm{C\,II}]\mathrm{u}}$), is calculated based on a two-level system (Draine 2010). We show the emissivity ratio in Figure 7 for two metallicities. As nitrogen is a secondary nucleosynthesis element, its elemental abundance increases nonlinearly with

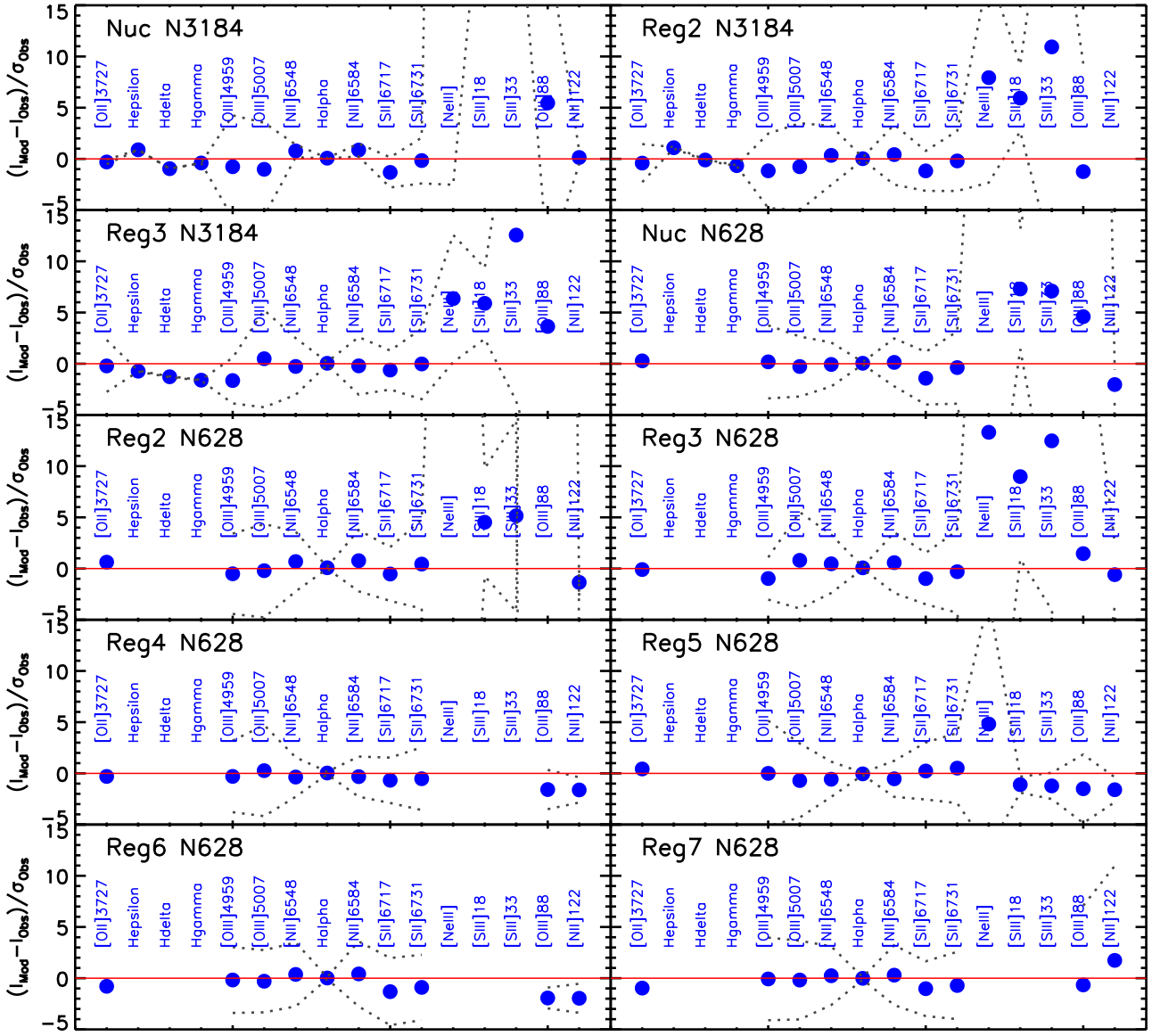

Figure 6. Comparison of line fluxes between the best-fit MAPPINGS model and the observed values (all lines normalized to Hβ). The solid red line indicates where the agreement between model and observations is best; the dash-dotted line indicates the 3σ uncertainties of the model. The extinction-corrected Hβ maps have been convolved to match the beam of the corresponding IRS or PACS spectroscopy beam size assuming a Gaussian profile. Reg4, Reg6, and Reg7 in NGC 628 are regions with no IRS observation.

metallicity in environments of high metallicity (Dopita et al. 2000). The variation in the line ratio reflects the difference in critical densities for these two transitions. We use the metallicities that we derived in Section 4.1. For 1 $Z_{\odot}$ C/H $= 2.57 \times 10^{-4}$, N/H $= 6.03 \times 10^{-4}$ and for 2 $Z_{\odot}$ C/H $= 9.10 \times 10^{-4}$ N/H $= 2.09 \times 10^{-4}$). We assume that the mixing of metals is very efficient in the regions, which may not be accurate on small scales (O'Dell et al. 2011; Lebouteiller et al. 2013). We assume $T_e = 7500$ K (Haffner et al. 2009).

Since we do not have [N II] 205 data for our regions to estimate the electron densities from the ratio of the [N II] 205 and [N II] 122 lines, we have two options. Haffner et al. (2009) quote emission measure values of ~10–60 cm^{-6} pc for the WIM in galaxies. In the low-density limit, we can calculate the emission measured from the observed [N II] flux, assuming that it fills the beam and that the nitrogen abundance is representative of the metallicity. Assuming a scale length given

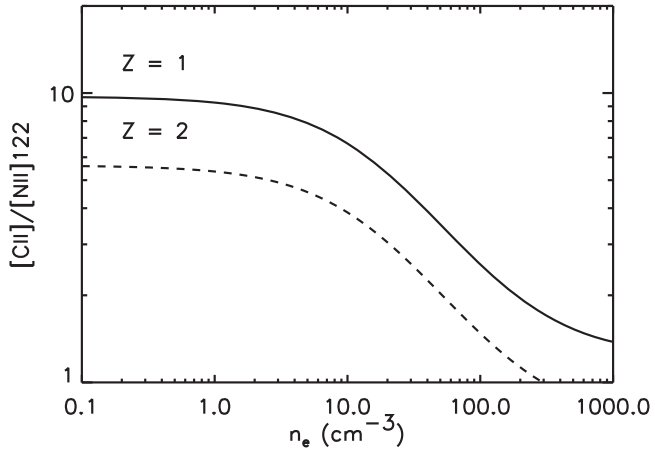

Figure 7. Emissivity ratio of [C II]/ [N II] 122 as a function of electron density for gas-phase metal abundances of 1 (solid black line) and 2 (dashed black line) $Z_{\odot}$.

by the beam size, we arrive at rms densities ranging from 1.6 to 3 cm^{-3}. These values are an order of magnitude higher than the typical WIM densities found by Monnet (1971), Reynolds (1991), and Haffner et al. (2009), which are in the range of 0.1–0.5 cm^{-3}.

Our result indicates that some fraction of the [N II]122 emission also arises from dense H II regions. In fact, some Hα, [O II]3727, [N II]6548, [N II]6584, and [S II]6717, [S II]6731 also arises from the WIM. From analytical calculation assuming $n_e = 0.1$ cm^{-3}, we found that the Hα flux from WIM is typically lower by three orders of magnitude than Hα from H II regions. We calculate that the observed ratio of [S II] over Hα and [N II] over Hα is lower by a factor of 10 than the analytically calculated [S II] over Hα and [N II] over Hα. Based on this rationale, we do not correct the Hα and optical emission lines ([S II], [N II], [O II]) for the contribution from the WIM. Based on our data, the presence of a WIM phase cannot be proven observationally. The Wisconsin Hα Mapper (WHAM, Tufte et al. 1998, Reynolds et al. 2005) survey showed that the WIM gas is present at high latitudes of the Milky Way. Our selection criteria, which select bright H II regions, imply that integrating over the line of sight, the emission from H II regions dominates the WIM emission.

Before scaling the [C II] contribution to the observed [N II] flux, we recall that the higher critical density [N II]122 μm line [N II] arises predominantly from the denser H II region component. Hence, we use MAPPINGS to estimate the fraction of [N II]122 emission from H II regions and subtract it. The remaining [N II] 122 emission is then used to estimate the [C II] emission from the WIM.

Another option is to use the result of the Beyond The Peak survey (BtP). Herrera-Camus et al. (2016) used the [N II]122 and [N II]205 lines to derive the electron densities for the ionized gas for a subset of the KINGFISH galaxies. Their derived median density for the entire set of subgalactic regions is $n_e \sim 30$ cm^{-3}. Using an FIR color estimator from Herrera-Camus et al. (2016), we find that n_e ranges from 5 to 10 cm^{-3}, although with large uncertainties that are due to the scatter in the FIR–[N II]205 relation. Again, this value is higher than the above-mentioned densities of 0.1–0.5 cm^{-3} for classical WIM gas and is more characteristic of giant H II regions. Similar electron densities have been reported by the GOTC+ study of Goldsmith et al. (2015). The authors conducted a survey of several lines of sight in the Milky Way.

Following Haffner et al. (2009), we have adopted a typical WIM electron density of 0.1 cm^{-3} in our calculations (see Table 6). Figure 7 shows that the emissivity ratio is insensitive to the assumed electron density in the range of 0.1–2 cm^{-3} and not very sensitive even up to densities as high as $n_e \sim 30$ cm^{-3}. We assume a density of 30 cm^{-3} to estimate the uncertainty (see Section 4.6).

On average, we find a wide range of the [N II] arising from the H II region rather than the WIM. In Nuc. N3184 and Reg7 N628, the observed [N II] flux can even be fully reproduced by the H II region and there is no significant WIM contribution to [C II]. For regions Reg2 N3184 and Reg3 3184, for which we have no data on [N II], we assume a most likely WIM contribution given by the average of the other eight regions.

On average, our WIM model yields 40%—but with a wide range of 10%–90%—of the observed [C II] flux. Goldsmith et al. (2015) found that about 30%–50% of [C II] arises from ionized gas, and correlates with [N II]205 emission. This ionized gas has a density between that of H II regions and WIM. The main challenging aspect comes from distinguishing the WIM from the H II region contributions to the [N II] flux.

4.3. The Dense PDR

For PDRs, the [C II] surface brightness mainly depends on two parameters: the hydrogen density n_H, and the incident radiation field G_0.

The first parameter, the PDR density, can be obtained by assuming pressure equilibrium with the H II region and adopting an electron temperature of 8000 K for the H II region temperature. We derive the PDR gas temperature from the excitation diagram of H_2 S(0) and S(1) lines (Parmar et al. 1991; Sheffer et al. 2011), assuming an ortho-to-para ratio (OPR) of 3 (Burton et al. 1992). This adopted OPR ratio for both galaxies is in agreement with Roussel et al. 2007. The derived temperatures range from 160 to 300 K (Table 5), typical for PDRs (Habart et al. 2011; Sheffer et al. 2011). The derived hydrogen densities are quite high, (1.6×10^4 to 9.6×10^4 cm^{-3}), as the electron densities from the H II region are also high.

One way to estimate the second parameter, G_0, is from the total infrared (or stellar) luminosity L_{TIR} (L_{UV}) and from the distance from the FUV source. The second method of estimating G_0 is by measuring the absorbed bulk UV radiation of the central star by the ISM. We explain our method of deriving G_0 in more detail in Appendix A.2. In our further analysis, we have adopted the G_0 values derived from Hβ. We prefer this approach, which directly yields G_0, over the method of Aniano et al. (2012), which adopts a power-law distribution of U for the PDR component.

We use the PDR model of Kaufman et al. (2006) and Pound & Wolfire (2008) to derive the [C II] surface brightness of dense PDRs for the derived G_0 and n_H (Figure 8). However, the total contribution of dense PDRs to the observed [C II] emission depends on the beam filling factor, i.e., which fraction of the area corresponding to one resolution element is covered by dense PDRs. This beam filling factor can be estimated in three different ways.

The first method to determine the filling factor is by comparing the total UV radiation and the intercepted UV radiation by the dense PDR. Consider a PDR cloud of radius R_{PDR} at the distance $R_{H\,II}$ from the star (i.e., the radius of the H II region measured from the Hα emission). The fraction of the UV light intercepted by the PDR and transformed into the infrared is given by

$$f_{scale} = \frac{\pi \times R_{PDR}^2}{4\pi \times R_{H\,II}^2}. \quad (2)$$

If the PDR has a surface brightness in the line given by I_{line}, then the observer will see a line flux given by

$$F_{line} = \frac{\pi \times R_{PDR}^2}{D^2} \times I_{line} = f_{scale} \times \frac{4\pi \times R_{H\,II}^2}{D^2} \times I_{line}, \quad (3)$$

or equivalently, $I_{line}(obs) = f_{scale} \times I_{line}$. However, under specific assumptions, f_{scale} is also f_{PDR}. In the study of the dust emission in KINGFISH galaxies by Aniano et al. (2012), only a fraction of the L_{TIR} arises from dense PDRs. The authors defined this fraction as f_{PDR}. For a small PDR filling factor, typically between 0.1 and 0.3 (Aniano et al. 2012), the

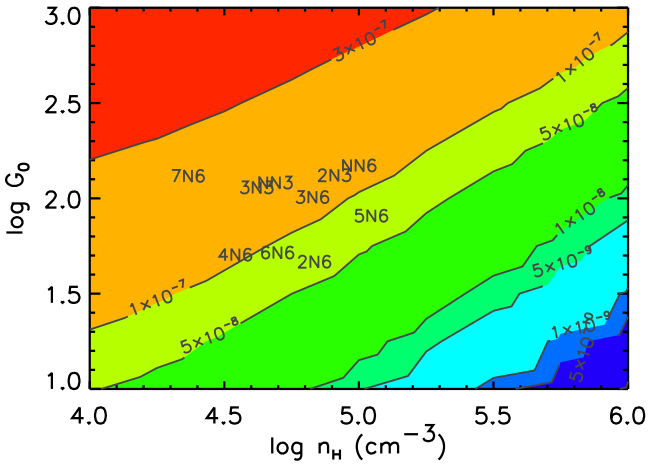

Figure 8. Contours of [C II] surface brightness as a function of G_0 and n_H (Kaufman et al. 2006; Pound & Wolfire 2008). Units are in W m^2 sr^{-1}. The surface brightnesses of [C II] are indicated as contours, and we added the region names in abbreviated form for better readability (2N6 corresponds to Region 2 in NGC 628, for instance). The expected [C II] emission from dense PDRs is calculated by multiplying the values in each region with f_{scale}.

contribution from the PDR to the total observed IR luminosity is small, but there is no discrepancy with the line-to-continuum ratio compared to models, i.e., with G_0 constrained from the stellar properties the PDR model can account for the line emission.

There are two key assumptions: first, the PDRs are at the typical distance of the size of the H II region (which is also the assumption that we use to derive the incident UV field). Second, the PDR surface seen by the star is the same as the surface area seen by the observer. An edge-on geometry will give a smaller surface area, but this reduction is compensated for by higher surface brightness. The [C II] surface brightness expected from dense PDRs has then accordingly to be scaled down by f_{PDR}. Hence, f_{PDR} may be considered a lower limit because in the optically thick environment of a dense PDR, the infrared radiation produced by absorption of UV photons can be processed by cooler dust deep inside the PDR (Hollenbach et al. 1991).

Second, given its high critical density and excitation energy, [O I] is an excellent tracer of dense PDRs (Beirão et al. 2012; Lebouteiller et al. 2012). We can estimate the beam filling factor from the [O I]63 μm emission by comparing the observed [O I]63 μm emission with the expected [O I]63 μm from the model as described below.

$$f_{scale} = \frac{I_{obs.}[\mathrm{O\,I}]63}{I_{model}[\mathrm{O\,I}]63}. \quad (4)$$

However, the strength of the [O I] line can be strongly affected by absorption in foreground gas (Kraemer et al. 1998; Vastel et al. 2001; Vasta et al. 2010). Indeed, Vasta et al. (2010) found in the study of 28 galaxies that about 20%–80% of [O I] flux is absorbed. We find that the filling factor derived from [O I] ranges from 0.005 to 0.03 with an average value of 0.02. These values are lower by a factor 13.5 on average than the f_{PDR} values. Recent observations of velocity-resolved [O I] have revealed the importance of absorption by cold foreground gas in dense PDR environments as well as the CNM (Leurini et al. 2015; Ossenkopf et al. 2015; Wiesemeyer et al. 2016). We attribute the large discrepancy between the [C II] fraction derived from the [O I] beam-filing factor and f_{PDR} to foreground absorption of [O I].

Third, PDRs are generally bright in the H_2 S(1) and S(0) lines (Sheffer et al. 2011; Sheffer & Wolfire 2013). Similarly to [O I], the beam filling factor can be calculated as

$$f_{scale} = \frac{I_{obs.}\mathrm{H_2}}{I_{model}\mathrm{H_2}}. \quad (5)$$

Here, the main uncertainty in the H_2 emission may arise from a possible contribution from shocks or turbulent dissipation in translucent clouds in the diffuse ISM (Ingalls et al. 2011), which are not included in our model. Comparing the observed intensities of H_2 S(1) and H_2 S(0) to our PDR model, we find that the intensity of H_2 S(0) can be fully accounted for without considering any shock contributions. This is also the case for the H_2 S(1) line in five regions (Reg2 N3184, Reg3 N3184, Nuc N628, Reg3 N628, and Reg5 N628). Only for the remaining two regions does the PDR model underpredict the observed H_2 S(1) line strength by factors of 2, approximately. The filling factor derived from the H_2 line ranges between 0.07 and 0.44 with an average value of 0.16. These values are similar to the filling factor derived from f_{PDR}.

While these estimates suggest that shocks and turbulent heating do not play a dominant role for the physical properties of our regions of interest, we cannot rule out minor contributions either. Hence we have decided against using the H_2 line as quantitative diagnostics. In principle, the [Si II] line can also be used as an indicator for the beam filling factor, but because this line can also have a large contribution from ionized gas (Abel et al. 2005; Kaufman et al. 2006), we do not consider it here.

Considering the disadvantage of several dense PDR tracers as explained above, we decided to scale the [C II] from the model with f_{PDR}. We emphasize that the interpretation of f_{PDR} as a beam filling factor is justified for our selected H II region-dominated regions where the TIR emission arises predominantly from UV flux converted by dust (see Figure 2). For regions dominated by the diffuse ISM, older stars would contribute a significant fraction to the TIR. In our regions, this contribution is very small and therefore neglected.

The [C II] emission from the dense PDR is then calculated from the [C II] surface brightness in Figure 8, multiplied by f_{PDR}. Perusing the values in Table 6, our model can explain the majority of 68% on average (40%–100%) of the observed [C II] emission coming from dense PDRs.

4.4. Surface of Molecular Clouds

The main difference between the surface of molecular clouds and the dense PDRs lies in the adopted density n_H, the strength of the illuminating radiation field G_0, and the beam filling factor. In comparison to dense PDRs, SfMCs have a much lower density and are irradiated by lower G_0, but they are more extended, leading to significantly larger beam filling factors. Since we do not have a suitable tracer of density, we assume $n_H = 300$ cm^{-3} for the SfMCs, in good agreement with Pineda et al. (2013) and Battisti & Heyer (2014).

We emphasize that the above-mentioned density of the SfMC differs from the densities we assumed for other ISM components (see Table 1). However, the entire ISM is not in thermal pressure equilibrium, which is mainly relevant for the diffuse gas. The thermal pressure on the SfMCs can be higher

than the thermal pressure in the diffuse gas because the molecular clouds are gravitationally bound. If the gas is converted into WNM, then the thermal pressure could be sufficiently high for the gas to evaporate, but this would only occur in hot spots near H II regions.

We furthermore assume that the SfMCs are irradiated by an average radiation field, whose strength we estimate from the dust model of Aniano et al. (2012). We use their dust maps for NGC 3184 and NGC 628, which have been derived from the dust model of Draine & Li (2007). This model considers two ISM components that contribute to the FIR color temperature: the first component is the diffuse medium as characterized by the Mathis field (Mathis et al. 1983) with a minimum U value (scaling factor of Mathis field). The second component has a radiation field that is characterized by a power law as a function of U. This dust-fitting model was applied to all KINGFISH maps on a pixel-by-pixel basis (see Aniano et al. 2012 for details).

We use the minimum U value and convert it into G_0 by multiplication with the factor 1.14 to convert the Mathis field into the Habing field. We list these G_0, notated as "G_0 dust," in Table 5. The observed FIR color temperatures of these regions indicate low incident radiation fields, $G_0 = 1.7$–3.4 (Aniano et al. 2012). The adopted G_0 values compare well with the finding of the GOTC+ study (Pineda et al. 2013), which derived G_0 between 1 and 30 for the surface of molecular clouds in the Milky Way.

The beam filling factor of SfMCs can be estimated using the CO emission as a tracer. Stacey et al. (1985), Shibai et al. (1991), Pineda et al. (2013), and Orr et al. (2014) showed that SfMCs are well traced by CO($J = 1 \rightarrow 0$). On galactic scales, CO($J = 1 \rightarrow 0$) correlates well with the CO($J = 2 \rightarrow 1$) emission (Braine et al. 1993; Leroy et al. 2009). We note that the dense PDR component will also contribute to the observed CO($J = 2 \rightarrow 1$) emission. Our models yield that the expected CO($J = 2 \rightarrow 1$) surface brightness of dense PDRs is an order of magnitude higher than that of SfMCs. The emission of CO($J = 2 \rightarrow 1$), estimated from dense PDRs after multiplication with the PDR filling factor (0.1–0.3), ranges from (1–4) $\times 10^{-10}$ W m^{-2} sr^{-1}, with an average value of $\sim$2.6 $\times 10^{-10}$ W m^{-2} sr^{-1}. The model is higher by a factor of 4 than the observed CO, hence the observed CO must rise from lower G_0 and n_H gas than our dense PDR. On the other hand, CO($J = 2 \rightarrow 1$) from modeled SfMCs is on average 1 $\times 10^{-10}$ W m^{-2} sr^{-1}. When we scale the modeled CO($J = 2 \rightarrow 1$) from SfMCs down by 1-f_{PDR}, we find that the modeled and observed CO($J = 2 \rightarrow 1$) differs by factor of 1.5. This implies that CO($J = 2 \rightarrow 1$ from the SfMC occupies a smaller beam filling factor than 1-f_{PDR}. Our investigation scale (500–600 pc) does not guarantee that dense PDR and the SfMC occupy a similar distance, however, hence using 1-f_{PDR} as a beam filling factor for CO is problematic.

Unfortunately, we do not have a better tracer of SfMCs than CO($J = 2 \rightarrow 1$) and do not have means to distinguish the dense PDR and SfMCs contribution to the observed CO($J = 2 \rightarrow 1$). Our assumption that CO($J = 2 \rightarrow 1$) mainly rises from the surface of molecular clouds is based on the recent study of Pineda et al. (2013) and Orr et al. (2014). The derived contribution of SfMCs to the observed [C II] emission is therefore an upper limit.

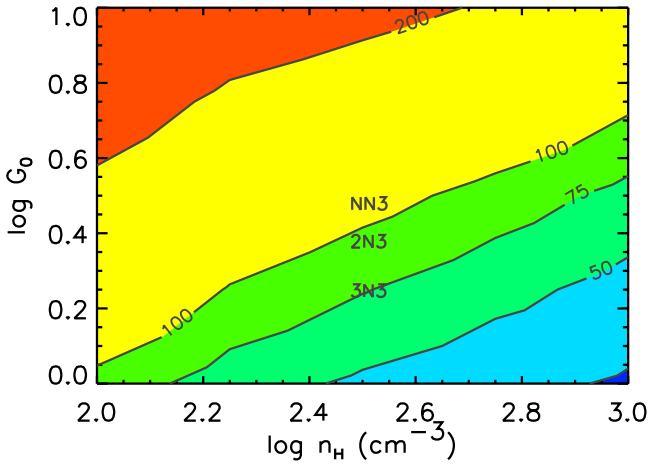

Figure 9. [C II]/CO($J = 2 \rightarrow 1$) from the surface of molecular clouds from Kaufman et al. (2006) and Pound & Wolfire (2008). We assume n_H=300 cm^{-3} at the surface, and we use the G_0 from Aniano et al. (2012). The contours are the ratios of [C II] over CO($J = 2 \rightarrow 1$) for the given G_0 and n_H. We selected four regions to represent the spread in parameters and the resulting variation in [C II] / CO($J = 2 \rightarrow 1$).

Since the range in physical and chemical conditions between dense PDRs and SfMCs overlaps, we expect some fraction of the [O I] emission and H_2 also to arise from SfMCs. We find that SfMCs can produce on average $\sim$15% of the observed [O I] and H_2.

As for dense PDRs, the physics, chemistry, and emission characteristics of SfMCs can be described by PDR models, with G_0 obtained from the dust model and the assumed n_H as input. We used the PDR model of Kaufman et al. (2006) and Pound & Wolfire (2008) to calculate the CO($J = 2 \rightarrow 1$) and [C II] emission from this component (see Figure 9), and then compared it to the observed CO($J = 2 \rightarrow 1$) to obtain the expected [C II] emission from SfMsCs (Figure 9).

We find that the modeled contribution from SfMCs to the observed [C II] flux ranges from 4% to 60% (Table 6). This large range in the fraction of [C II] reflects the large variation in the observed CO($J = 2 \rightarrow 1$) surface brightness (see Table 4).

4.5. CNM

The CNM is usually well traced by the H I 21 cm emission. We use data from The H I Nearby Galaxy Survey (THINGS, Walter et al. (2008) to derive the H I mass, brightness temperature T_B, and hydrogen column density N_H for each of our regions, following the prescription by Walter et al. (2008). The resulting H I parameters are listed in Table 5.

We note that not all of the detected H I is in the CNM phase. Following the study of H I emission in the Milky Way by Heiles & Troland (2003), we make the assumption that only one-third of the H I comes from the CNM, while two-thirds are in the WNM. We reduced the H I mass accordingly. We do not separately account for the WNM contribution to the [C II] emission, as this contribution—per H-atom—is a factor of ten smaller for the WNM than for the CNM (Wolfire et al. 1995). For the assumed CNM mass fraction, the [C II] contribution from the WNM contributes less than 20% of CNM values, which itself is a rather small contribution (see below). Therefore, we decided to neglect the contribution from the WNM.

Table 4
Photometric and Spectroscopic Data of Ten Regions in NGC 3184 and NGC 628

Region	Nuc. N3184	Reg2 N3184	Reg3 N3184	Nuc. N628	Reg2 N628	Reg3 N628	Reg4 N628	Reg5 N628	Reg6 N628	Reg7 N628	
R.A. J(2000)	154.5708	154.5344	154.5392	24.1738	24.1710	24.1768	24.1562	24.1891	24.1616	24.1664	
Decl. J(2000)	41.4241	41.4445	41.4406	15.7834	15.7849	15.7823	15.7528	15.7959	15.7401	15.7402	Reference
Band											
Photometry											
(MJy sr^{-1})											
IRAC 7.9	5.0 ± 0.5	1.7 ± 0.17	1.5 ± 0.15	3.4 ± 0.3	3.8 ± 0.4	4.0 ± 0.4	2.6 ± 0.3	3.3 ± 0.3	2.7 ± 0.3	1.9 ± 0.2	(1)
MIPS 24	5.5 ± 0.6	0.9 ± 0.1	1.2 ± 0.1	3.1 ± 0.3	4.4 ± 0.4	3.9 ± 0.4	8.9 ± 0.9	16.0 ± 0.1	10.5 ± 1.0	2.7 ± 0.3	(1)
PACS 70	153.9 ± 15.4	23.5 ± 2.4	20.2 ± 2.0	57.4 ± 5.7	66.3 ± 6.6	70.9 ± 0.8	53.8 ± 5.4	101.3 ± 10.1	76.0 ± 0.7	43.8 ± 0.4	(2)
PACS 100	241.4 ± 24.0	46.5 ± 4.6	43.9 ± 4.4	110.3 ± 11.0	128.9 ± 13.0	140.1 ± 14.0	78.4 ± 7.8	142.3 ± 14.2	105.3 ± 10.5	70.7 ± 7.0	(2)
PACS 160	231.8 ± 23.1	58.4 ± 6.0	56.7 ± 5.7	121.6 ± 12.1	153.1 ± 15.3	158.6 ± 15.7	78.7 ± 7.9	136.7 ± 13.7	105.3 ± 10.5	94.6 ± 9.4	(2)
TIR 10^{-6} W m^{-2} sr^{-1})	13.1	2.9	2.5	6.4	7.7	8.0	6.0	10.0	7.7	4.7	
PINGS Spectroscopy											
(10^{-8} W m^{-2} sr^{-1})											
[O II] 3727	6 ± 2	2.7 ± 0.8	1.9 ± 0.5	0.4 ± 0.08	0.3 ± 0.07	0.3 ± 0.1	4.2 ± 0.8	6.8 ± 1.4	9.6 ± 2	2.7 ± 0.5	(3)
Hϵ 3970	1.3 ± 0.2	0.1 ± 0.03	0.2 ± 0.04	NA	NA	NA	NA	NA	NA	NA	(3)
Hδ 4101	3.4 ± 0.7	0.3 ± 0.06	0.4 ± 0.09	NA	NA	NA	NA	NA	NA	NA	(3)
Hγ 4340	5.3 ± 1.0	0.7 ± 0.1	0.9 ± 0.2	NA	NA	NA	NA	NA	NA	NA	(3)
Hβ 4861	9.7 ± 1.9	1.2 ± 0.2	1.1 ± 0.2	0.7 ± 0.1	0.7 ± 0.2	0.5 ± 0.1	2.3 ± 0.5	3.2 ± 0.4	5.2 ± 1.0	1.1 ± 0.2	(3)
[O III]4959	0.5 ± 0.1	0.3 ± 0.5	0.2 ± 0.05	0.08 ± 0.01	0.04 ± 0.01	0.06 ± 0.02	0.3 ± 0.02	0.6 ± 0.1	2.6 ± 0.07	0.2 ± 0.04	(3)
O III] 5007	1.5 ± 0.3	0.7 ± 0.1	0.3 ± 0.06	0.3 ± 0.06	0.1 ± 0.02	0.07 ± 0.03	0.7 ± 0.04	2.4 ± 0.5	7.9 ± 1.6	0.6 ± 0.1	(3)
[N II] 6548	3.2 ± 0.6	0.4 ± 0.07	0.4 ± 0.07	0.09 ± 0.02	0.2 ± 0.05	0.2 ± 0.05	0.8 ± 0.05	1.9 ± 0.4	0.9 ± 0.3	0.2 ± 0.05	(3)
A(Hα)[a]	0.2	0.1	0.2	0.1	0.2	0.2	0.1	0.4	0.1	0.3	
Hα 6563	28.9 ± 5.8	3.6 ± 0.7	3.3 ± 0.7	0.8 ± 0.2	2.1 ± 0.5	1.6 ± 0.5	6.8 ± 0.4	15.4 ± 3.1	15.1 ± 3.0	3.3 ± 0.6	(3)
[N II] 6584	9.1 ± 1.8	1.1 ± 0.2	1.0 ± 0.2	0.2 ± 0.05	0.6 ± 0.2	0.5 ± 0.2	2.3 ± 0.2	5.7 ± 1.1	2.6 ± 0.5	0.7 ± 0.1	(3)
[S II] 6717	3.9 ± 0.8	0.6 ± 0.1	0.5 ± 0.1	0.1 ± 0.02	0.2 ± 0.06	0.2 ± 0.06	1.1 ± 0.07	1.6 ± 0.1	1.4 ± 0.3	0.5 ± 0.1	(3)
[S II] 6731	2.9 ± 0.6	0.4 ± 0.08	0.3 ± 0.06	0.08 ± 0.02	0.2 ± 0.04	0.1 ± 0.05	0.8 ± 0.05	1.2 ± 0.1	1.0 ± 0.3	0.3 ± 0.06	(3)
LL IRS Spectroscopy											
[Ne III] 15.6	0.2 ± 0.09	0.1 ± 0.03	0.1 ± 0.03	0.06 ± 0.02	0.05 ± 0.01	0.08 ± 0.02	NA	0.3 ± 0.1	NA	NA	(4)
H_2(0,0) (S1) 17.0	0.5 ± 0.01	(0.1 ± 0.1)	0.1 ± 0.03	0.09 ± 0.03	0.05 ± 0.01	0.08 ± 0.02	NA	0.02 ± 0.006	NA	NA	(4)
[S III] 18.7	1.2 ± 0.1	0.3 ± 0.1	0.3 ± 0.1	0.2 ± 0.06	0.4 ± 0.1	0.3 ± 0.1	NA	3.4 ± 1.0	NA	NA	(4)
H_2(0,0) (S0) 28.2	0.06 ± 0.02	(0.02 ± 0.01)	(0.02 ± 0.01)	(0.007 ± 0.003)	0.006 ± 0.002	0.01 ± 0.003	NA	0.05 ± 0.01	NA	NA	(4)
[S III] 33.5	1.3 ± 0.07	0.3 ± 0.07	0.3 ± 0.07	0.1 ± 0.03	0.4 ± 0.1	0.2 ± 0.06	NA	3.8 ± 2.0	NA	NA	(4)
[Si II] 34.8	2.2 ± 0.09	0.4 ± 0.09	0.3 ± 0.09	0.5 ± 0.1	0.9 ± 0.3	0.9 ± 0.3	NA	2.6 ± 0.6	NA	NA	(4)
PACS Spectroscopy											
[O I] 63	1.8 ± 0.04	0.4 ± 0.01	0.4 ± 0.04	(0.4 ± 0.2)	0.6 ± 0.2	0.5 ± 0.1	1.2 ± 0.2	2.1 ± 0.6	1.2 ± 0.2	0.5 ± 0.02	(2)
[O III] 88	0.5 ± 0.01	0.6 ± 0.01	0.4 ± 0.03	0.03 ± 0.01	0.01 ± 0.003	0.1 ± 0.03	0.9 ± 0.1	2.2 ± 0.04	4.7 ± 0.004	(0.8 ± 0.3)	(2)
[N II] 122	(0.8 ± 0.3)	NA	NA	(0.2 ± 0.08)	(0.2 ± 0.07)	(0.1 ± 0.07)	(0.2 ± 0.07)	0.6 ± 0.1	(0.2 ± 0.07)	(0.03 ± 0.01)	(2)
[C II] 158	4.8 ± 0.1	1.8 ± 0.3	1.8 ± 0.4	1.8 ± 0.1	2.2 ± 0.1	1.9 ± 0.1	3.1 ± 0.1	3.5 ± 0.1	3.4 ± 0.1	2.3 ± 0.1	(2)
THINGS											
(Jy Km s^{-1})											
H I 21 cm	0.01	0.03	0.03	0.001	0.004	0.05	0.04	0.03	0.05	0.06	(5)
HERACLES											
(10^{-10} W m^{-2} sr^{-1})											
CO(J=2 − 1)	7.0 ± 0.2	0.6 ± 0.1	2.4 ± 0.1	0.6 ± 0.1	0.7 ± 0.2	0.6 ± 0.1	0.2 ± 0.0	0.7 ± 0.1	0.3 ± 0.0	0.2 ± 0.2	(6)

Notes. The surface brightness values in brackets are lower than 3σ, and we include these values as upper limits in our analysis.
[a] The extinction correction for Hα.
References. (1). Gil de Paz et al. (2007), (2). Kennicutt et al. (2011), (3). Rosales-Ortega et al. (2010), (4). Kennicutt et al. (2003), (5). Walter et al. (2008), (6). Leroy et al. (2009).

Table 5
Region Properties

Region	Nuc. N3184	Reg2 N3184	Reg3 N3184	Nuc. N628	Reg2 N628	Reg3 N628	Reg4 N628	Reg5 N628	Reg6 N628	Reg7 N628
n_e (cm^{-3})[a]	1000, 700 ± 200	1000,700 ± 300	300, 600 ± 300	3000, 1600 ± 1000	1000, 1100 ± 300	1000, 850 ± 800	300, 600 ± 200	300, 750 ± 200	1000, 700 ± 300	300, 300 ± 10
q (10^7 cm s^{-1})[a]	1,2	1,1.7	1,1.4	1.6,4	1,1.7	1.6,1.7	1,1.4	1,2	4,4	1.6,1.7
Z ($Z_\odot$)	2	1	1	1	2	2	1	1	1	1
NLyC (s^{-1})[b]	$10^{51.93\pm0.14}$	$10^{51.03\pm0.09}$	$10^{50.99\pm0.12}$	$10^{50.37\pm0.21}$	$10^{50.40\pm0.18}$	$10^{50.26\pm0.06}$	$10^{50.91\pm0.62}$	$10^{51.24\pm0.07}$	$10^{51.25\pm0.1}$	$10^{50.57\pm0.18}$
$R_{H\ II}$ (pc)	170	58	59	26	47	27	80	94	118	34
L_{Bol} (10^6 $L_\odot$)	910.1	104.5	102.1	4.6	60.1	36.2	67.5	262.5	102.1	57.4
L_{UV}(10^6 $L_\odot$)[c]	159.3	20.3	18.2	4.4	4.7	3.4	14.98	32.74	33.01	7.03
L_{TIR} (10^6 $L_\odot$)[d]	70	15	13	24	28	30	22	38	28	17
f_{PDR} [e]	0.23	0.10	0.10	0.07	0.10	0.08	0.30	0.30	0.30	0.10
T_{gas} (K)[f]	304	188	224	390	300	250	300	100	300	300
n_H (10^4 cm^{-3})[g]	4.2	6.8	3.6	8.6	5.9	5.7	2.7	9.6	4.3	1.6
G_0 L_{UV}[h]	112.5	122.9	106.1	138.3	43.3	94.4	47.1	75.3	48.3	121.9
G_0 L_{TIR}[i]	49.4	91	76.2	478.1	164.1	529.4	43.9	55.7	26	187.6
G_0 dust[j]	2.9 ± 1.6	2.3 ± 1.0	1.7 ± 0.7	2.3 ± 1.1	1.9 ± 0.9	2.3 ± 1.1	3.4 ± 1.6	2.3 ± 1.0	3.4 ± 1.5	2.3 ± 1.1
N_H (10^{21} cm^{-2})[k]	4.1	13.2	12.6	0.2	1.1	1.6	11.3	7.6	14.1	18.8
SFR ($M_{yr^{-1}}$)[l]	24.7	3.9	3.0	0.4	0.5	0.5	1.1	2.0	1.3	0.3

Notes.
[a] Electron density of the H II region. The first value derived from MAPPINGS, the second value from averaged [S II]6717, 6731 and [S III]18, 33.
[b] From Hβ.
[c] Energy calculated in the range of 6–13.6 eV.
[d] Derived using relation in Draine & Li (2007).
[e] f_{pdr} = fraction of L_{TIR} that comes from $U \geqslant 100$ (Aniano et al. 2012).
[f] Gas temperature for the dense PDR derived from H_2 S(0) and S(1).
[g] Hydrogen density for the dense PDR derived from the pressure equilibrium assumption.
[h] Derived from L_{UV}, see Equation (7).
[i] Derived from L_{TIR}, see Equation (7).
[j] From the dust model of Aniano et al. (2012).
[k] The atomic hydrogen column density derived from H I.
[l] Derived using the relation in Kennicutt et al. (2009).

Table 6
Modeled and Normalized Fractions of the Observed [C II] Flux from Each of the Five ISM Phases

Region	Dense H II	WIM[a]	Dense PDR	SfMC[b]	CNM	Total	Modeled [C II] 10^{-8} W m^2 sr^{-1}
Nuc. N3184	0.2 ± 0.03	0.0	0.9 ± 0.05	1.6 ± 0.7	0.02 ± 0.01	2.7 ± 0.7	12.9
	0.07	0.0	0.33	0.59	0.01		
Reg2 N3184	0.03 ± 0.01	0.3*	0.7 ± 0.1	0.2 ± 0.1	0.1 ± 0.1	1.3 ± 0.3	2.5
	0.02	0.28	0.50	0.14	0.07		
Reg3 N3184	0.07 ± 0.04	0.3*	1.0 ± 0.5	0.9 ± 0.6	0.1 ± 0.05	2.4 ± 0.6	4.3
	0.03	0.17	0.42	0.38	0.04		
Nuc. N628	0.01 ± 0.01	0.4–0.9	0.4 ± 0.2	0.2 ± 0.1	0.003 ± 0.001	1.5 ± 0.2	2.7
	0.007	0.60	0.27	0.13	0.002		
Reg2 N628	0.02 ± 0.02	0.1–0.2	0.2 ± 0.1	0.1 ± 0.1	0.01 ± 0.005	0.5 ± 0.2	1.4
	0.03	0.31	0.31	0.31	0.02		
Reg3 N628	0.01 ± 0.02	0.07–0.1	0.6 ± 0.1	0.2 ± 0.1	0.01 ± 0.005	0.9 ± 0.2	1.7
	0.01	0.11	0.67	0.22	0.01		
Reg4 N628	0.04 ± 0.02	0.07–0.1	0.9 ± 0.03	0.07 ± 0.03	0.06 ± 0.03	1.2 ± 0.1	3.7
	0.04	0.1	0.90	0.07	0.06		
Reg5 N628	0.2 ± 0.08	0.3–0.7	0.5 ± 0.1	0.1 ± 0.08	0.04 ± 0.02	1.5 ± 0.3	5.3
	0.13	0.45	0.32	0.06	0.03		
Reg6 N628	0.02 ± 0.005	0.2–0.3	0.7 ± 0.1	0.1 ± 0.04	0.1 ± 0.04	1.2 ± 0.2	4.1
	0.02	0.25	0.57	0.08	0.08		
Reg7 N628	0.03 ± 0.03	0.0	0.9 ± 0.2	0.06 ± 0.04	0.1 ± 0.06	1.0 ± 0.1	2.9
	0.03	0.0	0.82	0.05	0.09		
Plain average	0.06	0.31	0.68	0.35	0.05	1.45	
Normalized mean	0.04	0.21	0.47	0.24	0.03	1.0	

Note. The values in columns 2 through 6 are the modeled fractions of the observed [C II] flux from each ISM phase. Column 7 lists the sum of the individually modeled [C II] fluxes with respect to the observed values. The total modeled flux is listed in column 8. On average, the sum of the modeled fluxes exceeds the observed value by 40%. In order to match the observed value, the individual model values have been normalized and are listed in the columns below each region (numbers without unvcertainties), see Section 5.3. Numbers marked with an asterisk have been derived by adopting the median value across all regions as no observational data were available. The values in a column marked with a superscript a are upper limit calculations as the assumed lowest density gives the highest [C II]. The values in column marked with a superscript b are upper limits as CO($J = 2 \rightarrow 1$) used to scale the [C II] can arise from dense PDR.

In order to estimate the total [C II] emission, we multiplied the resulting $N_{\rm H}$ with the appropriate cooling rate, taken from Wolfire et al. (1995). The cooling rate per hydrogen nucleus is a function of thermal pressure P/k and G_0. Analogous to the SfMCs, we adopted the minimum U (see Section 4.4) for each region as derived from the dust model of Aniano et al. (2012). We assumed that the ISM gas pressure in these galaxies is similar to the pressure derived for the Milky Way through UV absorption lines of [C I] (Jenkins & Tripp 2011) and in the recent GOTC+ study of the [C II]158 μm line (Pineda et al. 2013), with $P/k \sim$ 1000–3000 K cm^{-3}. As expected, these thermal pressures are lower than those in the H II regions and PDRs (Table 1) by several orders of magnitude. We adopted $P/k \sim 2000$ K cm^{-3} for the extra-nuclear regions, and following Wolfire et al. (2003), the higher value of $P/k \sim$ 10,000 K cm^{-3} for the nuclear regions. This results in a cooling rate of 6.2×10^{-26} erg/s/H for the extra-nuclear regions and 11×10^{-26} erg/s/H for the nuclear regions.

These values are somewhat higher than the average cooling rate observed by COBE for the Milky Way ($\sim 2.65 \pm 0.15 \times 10^{-26}$ erg/s/H; Bennett et al. 1994) and by *ISO* for the spiral arms in M31 (2.7×10^{-26} erg/s/H; Rodriguez-Fernandez et al. 2006). However, this apparent discrepancy merely reflects the fact that Bennett et al. (1994) did not correct for the WNM contribution when calculating the [C II] cooling rate per H-atom.

Even with our higher values for the cooling rate, our model predicts rather small [C II] contributions from the CNM, ranging from 0.3% to 10% (Table 6). We found that the [C II] fraction from CNM has an uncertainty ~30%, but because the [C II] fraction from CNM is small, this uncertainty is also small.

4.6. Quantifying the Uncertainties on the [C II] Fraction

We summarize the main uncertainties in our method on the derived [C II] fractions. Figure 10 summarizes our analysis and uncertainties.

The uncertainty of the [C II] fraction from H II region is calculated by propagating the model grid and the observational uncertainty. If the densities were much lower than the optical lines indicates, the contribution from H II regions to the observed [C II] would be concomitantly larger. For an electron density of only $n_e = 100$ cm^{-3}, the [C II] fractions from our selected regions would increase by factors ranging from 2 to 20, with a linear average of 8. In all cases, however, would the H II regions remain a minor [C II] contributor with fractions well below 25%. The uncertainty in the [C II] emission from the H II regions is estimated from the model grid study when we consider models with $\chi 2$ within a factor of two of the best fit.

The uncertainty from WIM components mainly rises from the electron density assumed. If we adopt the low ionized gas density from Herrera-Camus et al. (2015) (30 cm^{-3}), then the [C II] fraction will be lower by a factor of two than the current value. The uncertainty of the [C II] fraction from the WIM is calculated by contrasting the different electron densities ($n_{\rm e} = 0.1$ and $n_{\rm e} = 30$ cm^{-3}).

The uncertainty in the [C II] fraction from dense PDR is set by G_0 and $n_{\rm H}$. The uncertainty of $n_{\rm H}$ is propagated from $n_{\rm e}$ in the H II regions, while the G_0 uncertainty is adopted from the difference between G_0 derived from $L_{\rm TIR}$ and from $L_{\rm UV}$. We

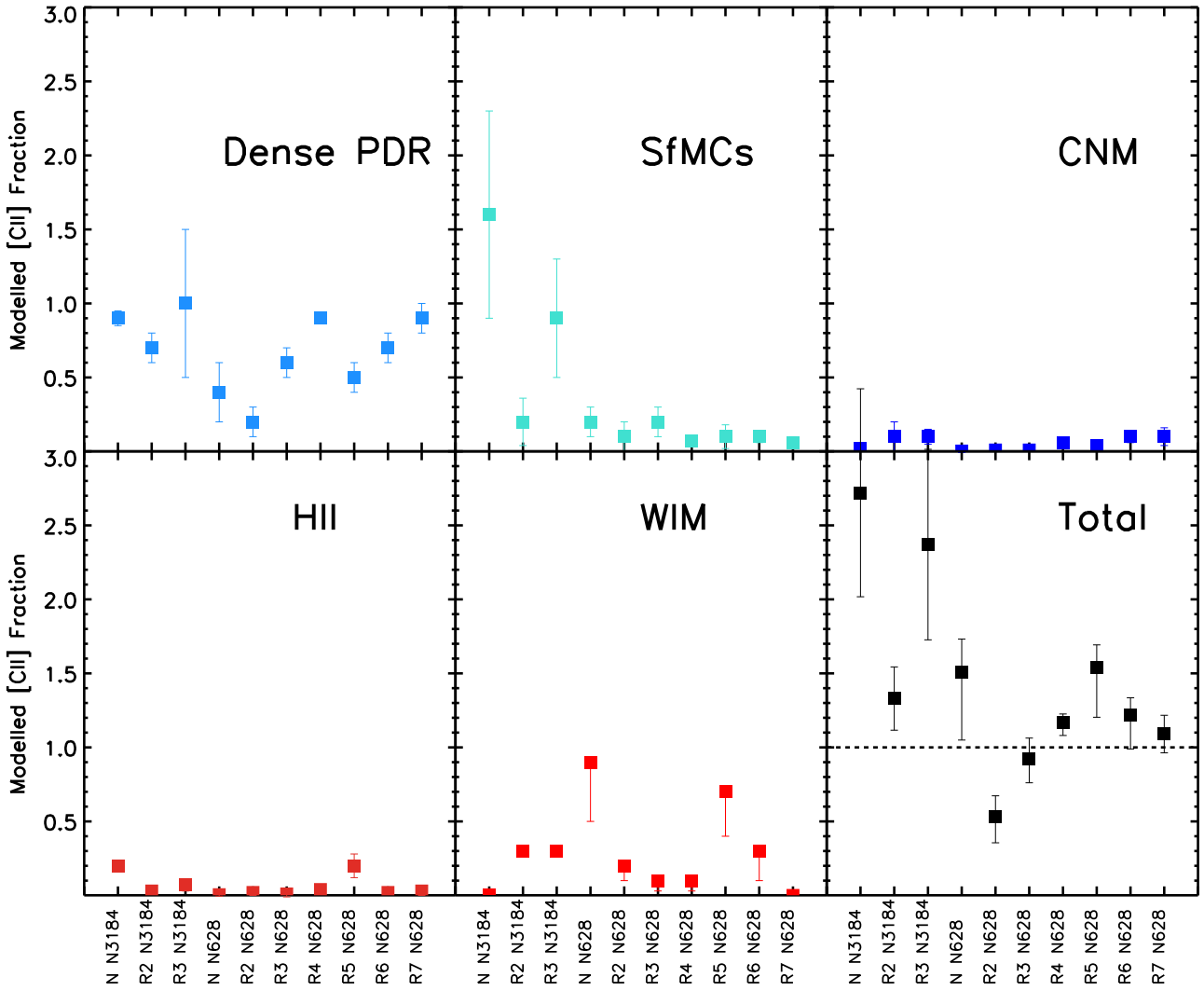

Figure 10. Bar diagram with the contributions to [C II] from each of the five phases. For Reg2 and Reg3 in NGC 3184 no WIM tracer is available and we have adopted the [C II] fraction derived from the median value of other regions (see Table 6 for details). The black dashed line is the observed value of [C II].

calculate the uncertainty of the [C II] fraction by propagating the uncertainty of $n_{\rm H}$ and G_0. Another uncertainty is the radius of the H II region ($R_{\rm H\,II}$). If we eliminate the dependency on $R_{\rm H\,II}$, i.e., using a dimensionless q parameter from MAPPINGS to derive G_0, the derived G_0 would be on average about three times lower (albeit with larger scatter) than G_0 from $L_{\rm UV}$. While this would reduce the [C II] fraction from dense PDRs in some but not all of our selected regions, the main conclusion, namely that dense PDRs are the dominating contributor to the [C II] emission, remains unaffected.

For SfMCs, the uncertainty of [C II] fraction is calculated from the uncertainty of G_0 derived from the dust map and the gas density. On average, G_0 is uncertain by about ∼50%. This translates into an uncertainty in the [C II] fraction by factor of 1.4 on average. The main uncertainty comes from the dense PDR contribution to the CO($J = 2 \rightarrow 1$) flux. We derived the uncertainty of the gas density from the density distribution of molecular clouds, which ranges from 100–500 $\rm cm^{-3}$ (Battisti & Heyer 2014). The uncertainty in the density translates into an uncertainty of the [C II] fraction of ∼80%. As we explained in Section 4.4, the calculation of the [C II] fraction of SfMCs is an upper limit.

The CNM [C II] fraction is governed by the assumption of the CNM:WNM fraction and the thermal pressure. We adopted the observed average ratio of CNM:WNM = 1:2 from the study of Heiles & Troland (2003). In their survey of the [C II] emission in the Milky Way, Pineda et al. (2013) also arrived at an average CNM:WNM ∼1:2. The range in the ratio is also adopted from the work of Pineda et al. (2013), and the uncertainty in the fractional [C II] contribution from the CNM is ∼0.4. The cooling rate per hydrogen atom depends weakly on the gas thermal pressure. The ISM pressure measured by Pineda et al. (2013) for the Milky Way ranges from 1000 to 3000 K. These values are in good agreement with the [C I] study by Jenkins & Tripp (2011). We have adopted a thermal pressure of 2000 K $\rm cm^{-3}$ with an uncertainty of ±1000 K $\rm cm^{-3}$.

5. Discussion

In Section 4 we discussed how we independently derived the [C II] flux for each ISM phase in NGC 3184 and NGC 628. We summarize the model procedure in Figure 3 for convenience.

Now we combine the results from Section 4 to obtain the total [C II] flux for each of our ten distinct regions (Section 3.3)

within NGC 3184 and NGC 628. We then compare the observed [C II] flux densities to the sum of the modeled contributions. Obviously, if the sum of the independently modeled contributions does not come close to the observed [C II] strength, there would be little confidence in our model. On the other hand, given the theoretical and observational complexity of our model, an agreement within a factor of two could be considered a success and provides sufficient confidence in our model.

5.1. Main Results

The modeled fractions of the [C II] emission from the five ISM phases are listed in Table 6 for each of the ten regions within NGC 3184 and NGC 628. Table 6 also shows in its rightmost column the sum of the various contributions. For the subsequent discussion of the various regions, a graphical visualization of the numbers in Table 6 seems helpful. Hence, we converted them into a bar diagram, which is shown in Figure 10. Although the exact contributions vary from region to region, we can state two general findings.

First, our model reproduces the observed [C II] emission quite well. The exceptions are Nuc N3184, Reg3 N3184, Nuc N628, and Reg5 N628, and even there, the discrepancy is within a factor of two, for reasons that are further discussed in Section 5.2. Given the good match on one hand and the many largely independent observational and theoretical parameters (Figure 3) that enter our model on the other hand, we consider our approach to be quite successful. Second, although the exact contributions from each phase vary from region to region, there is an underlying trend that we discuss in Section 5.3.

Obviously, the uncertainties play an important role in the interpretation of the results. The uncertainties quoted in Table 6 include the observational errors as well as the systematic uncertainties. The latter vary in their reliability as diagnostic tracers. Generally speaking, the three phases, H II region, dense PDRs, and CNM, have relatively good tracers, leading to very well-constrained gas parameters. Unfortunately, this is not the case for the SfMC and WIM. As shown in Figure 10, the two phases have relatively large error bars and vary from region to region. More specifically, the main uncertainties for the [C II] from WIM arise from the uncertainties in electron density. The uncertainties of the [C II] fraction from dense PDR and the SfMC arise from densities and G_0. The uncertainties of the [C II] emission from CNM come from the thermal pressure in the CNM:WNM ratio. The total uncertainty quoted in Table 6 assumes that the individual uncertainties are mutually independent. While this is likely for most cases, it may not apply to the H II regions and dense PDRs, whose gas properties are linked.

Arguably the greatest uncertainty with regard to generalizing our results lies within the selection of our ten analyzed regions. As stated in Section 1.3, the unavoidable selection on the basis of sufficient S/N for spectroscopy introduces a bias toward regions of massive star formation. This bias is visualized in Figure 2, which shows the histograms of total infrared emission for each resolution element (beam) within both galaxies in comparison to the selected regions. It is obvious that the majority of regions (beams) have significantly lower TIR emissions than our selected regions. While this may not be a significant bias with respect to the study of the ISM in galaxies at higher redshift—which underlie similar selection biases due to S/N requirements—it is clear that our results do not describe the ISM in the more quiescent regions of normal galaxies, for which we would expect relatively higher contributions from the CNM and the SfMCs.

5.2. Results Region by Region

In regions Nuc N3184 and Reg3 N3184, we apparently overestimate the total [C II] emission by up to factor of 2, probably because of an overestimate of the contributions from SfMCs and WIM. Nuc N3184 and Reg3 N3184 show a two to three times higher contribution from SfMCs than the other regions. As discussed in Section 4.4, it is possible that part of the CO($J = 2 \rightarrow 1$) flux, which arises in dense PDRs, may be incorrectly attributed to SfMCs.

We underestimate the total [C II] in Reg2 of NGC 628, with our model yielding only 50% of the observed value. It might be that the missing [C II] emission comes from mechanisms that were not included in our model. For instance, Appleton et al. (2013) showed that the [C II] emission in Stephan's Quintet is greatly enhanced, most likely by shock-heated gas. However, we consider such a scenario unlikely for the reasons given in Section 4.3. Furthermore, the nuclei of NGC 628 and NGC 3184 host no active AGN (Moustakas et al. 2010) that could make a significant contribution, although there is a low-luminosity X-ray (XDR) region (Grier et al. 2011).

We might be missing [C II] from Reg2 of NGC 628 because hidden star-forming regions may be present. Reg2 is consistently bright in the 8, 24, 70, and 160 μm continuum images, but not in Hα. If the UV photons are directly and efficiently absorbed by thick layers of dust surrounding the H II region, our extinction correction is insufficient. Consequently, we underestimate G_0 and the [C II] strength from the dense PDR. If G_0 were underestimated by a factor of three, we would miss ~30% of the [C II] from dense PDRs for Reg2. In order to test this hypothesis, we checked the ratio of 24 μm over Hα, which is twice as high as the median value of the other regions, indicating that a substantial fraction of the star-forming regions is deeply buried in dust clouds. We do not consider the contribution from an older stellar population to the 24 μm flux (Leroy et al. 2012) to be significant because of our selection bias toward regions that are dominated by ongoing star formation.

5.3. The Dominating ISM Components

We have modeled the galactic ISM with five phases or components to estimate the [C II] emission. The results are presented in Table 6 as "plain average." Our comprehensive approach of modeling all relevant phases of the ISM has the additional advantage over studies of single ISM components of providing a cross-check: the sum of all phases should yield the observed [C II] flux. As can be seen from Table 6, this is, as expected, not exactly true. On average, the sum of the individually and independently modeled components is about 45% higher than the observed [C II] flux. Given the many observational and theoretical uncertainties and the fact that for both WIM and SfMCs we have only upper limits, we consider a mismatch of less than 50% as strong support for our approach.

We recall that our main goal is to quantify the relative contributions of the various phases and identify the dominating contributor(s). In order to make such statements, we have to

normalize the contributions to a total of unity. As an extreme example, it would not make physical sense to state that the strongest component produces 120% of the [C II] flux. This may lead to the incorrect conclusion that one single component would be sufficient to explain all of the observed [C II] flux, although [C II] emission from other components has been detected as well.

Since we have no exact knowledge of the systematic observational and theoretical uncertainties of the various methods, we assume that all methods suffer from the same systematic uncertainties. The resulting normalized values are also listed in Table 6 as "normalized mean." The discrepancy of 45% on average illustrates the inherent uncertainties. We therefore refrain from overstating the numbers per se, but instead focus on what the dominating, important, and minor contributors are. These conclusions do not depend critically on whether the results have been normalized.

In summary, we find (Table 6) that in most regions, dense PDRs are the dominating component, contributing about two-thirds of the [C II] flux on average. The second most important component s are the SfMCs and the WIM. On average, SfMCs and WIM components together account for about half of the contribution from dense PDRs. The WIM contribution shows the largest scatter between the individual regions. We emphasize again that both WIM and SfMCs are estimated from upper limits, but even for lower realistic estimates, our finding still holds that they are significant contributors to the [C II] flux. Finally, the contributions from dense H II regions and the CNM are rather minor, with less than 5% each. Including more phases in the model would likely not significantly affect the results.

5.4. Comparing Our Results to Other Studies

We now consider the individual phases in more detail, and compare our findings to results from the literature. We caution the reader to compare the numbers at face value, since many published values have been derived with different methods, often not clearly stating the systematic uncertainties. For instance, the term "PDR" is defined by different authors with very different G_0 and $n_{\rm H}$. Nevertheless, it is interesting to review the large scatter among the results in the literature.

K. V. Croxall et al. (2017, private communication) find, based on [N II]205 μm data from the BtP and the KINGFISH samples of numerous regions in several galaxies, that 84%, with 15% scatter, of [C II] emission arises from neutral gas, which includes in our notation the dense PDRs, the SfMCs, and the CNM. The remaining 16% arise from ionized gas, which includes our H II regions and WIM components. We obtained a neutral fraction (PDRs + SfMC + CNM) of 80%, which is roughly 5% lower but well within the range of the result of Croxall et al. (84%), derived in a completely different way. For comparison, Beirão et al. (2012) found in NGC 1097 that 3%–33% [C II] arises from ionized gas, and Croxall et al. (2012) found for NGC 4559 and NGC 1097 that the average ionized gas contribution to the [C II] emission is 20%–50%. Neither study distinguished between the contributions from diffuse and dense ionized gas.

We have seen that more than half of the [C II] emission comes from dense PDRs, with G_0 ranging from 50 to 150 and $n_{\rm H}$ of $\sim$(2–10) $\times$ 10^4 cm^{-3}. The star-forming regions that are bright in Hα—Nuc, Reg2, Reg3 in NGC 3184, and Reg4, Reg5, Reg6, and Reg7 in NGC 628—show the largest fractional contributions from PDR gas, about 50%. For comparison, Kapala et al. (2015) investigated several star-forming regions in M31 with 700 pc in physical size and 50 pc of resolution. They distinguished between star-forming and non-star-forming regions using a Hα threshold, and found that between 20% and 90% of the [C II] emission rises from non-star-forming regions, i.e regions or components other than H II regions and dense PDRs. Our selected regions are bright in Hα emission, indicating very high star-forming activity. Therefore, our finding that star-forming regions have a strong contribution from dense PDRs agrees with the conclusion drawn by Kapala et al. (2015).

Chevance et al. (2016) studied 30 Dor in the low-metallicity LMC as a template for H II extragalactic regions. The star-forming complex of 30 Dor has Lyα continuum photon fluxes that are comparable to our sample. Chevance et al. (2016) found that 90% of the [C II] emission in 30 Dor arises from PDRs with G_0 ranging from 100 to 2.5 $\times$ 10^4. Chevance et al. (2016) simulated 30 Dor at a large distance and found that the drop in G_0 will possibly bring the [C II] fraction from PDRs close to our result. Chevance et al. (2016) also found that the strongest cooling line of 30 Dor is [O III]88 and not [C II] because of the lower metallicity of 30 Dor.

Röllig et al. (2016) investigated regions of a few hundred parsecs in IC 342 by comparing the spectra of [C II] and [N II] 205 with CO, aiming to disentangling the emission from ionized and photodissociation regions. IC 342 was selected because of its distance and data completeness. Röllig et al. (2016) found that between 35% and 90% of the [C II] arises from ionized gas and that the central region shows a higher contribution from ionized gas. In comparison, our result that 3%–50% of the [C II] arises from WIM and H II regions is smaller by factor of two. Of two nucleus regions, only Nuc N628 shows a high fraction (43%) of ionized contribution to the [C II] emission. The studies by Röllig et al. (2016) and by Pineda et al. (2013) claimed that ionized gas might be an important [C II] contributor toward the central parsecs of IC 324 and the Milky Way, respectively. A larger sample of galactic nuclei is needed to verify this claim.

For the interior of the Milky Way, Pineda et al. (2013, 2014) sampled 425 lines of sight and found that PDRs with $n_{\rm H}$ $\sim$100–1000 cm^{-3}, located far away from massive star-forming regions (G_0 $\sim$ 1–30), contribute only up to 30%–47% to the total [C II]. They identified the PDR components from the presence of CO emission and [C II], which made no distinction between dense Orion-like PDRs and less intense PDRs. In fact, their PDR gas properties are rather similar to our SfMC component, for which we assumed G_0 $\sim$ 1–3 and $n_{\rm H}$ $\sim$1000 cm^{-3}. Comparing this result to Pineda et al. (2013, 2014), keeping in mind that our estimation is an upper limit for SfMCs, our approach yields lower [C II] contributions from the SfMCs than the studies of Pineda et al. (2013, 2014).

Concerning the contributions from H II regions, previous studies by Carral et al. (1994) and Kramer et al. (2005) yielded about 30% from H II regions on average. On the other hand, Pineda et al. (2013) found for regions in the Milky Way that only 4% of [C II] comes from ionized gas. Our findings of contributions of 4% on average agree well with the results of Pineda et al. (2013), although the assumptions on parameters like $n_{\rm e}$ affect the results considerably. We recall that our modeling uses a comprehensive set of optical emission lines to constrain the H II region properties.

Last, we found that the CNM component, with an average contribution of 4%, is not a very significant [C II] contributor in our star-formation-dominated regions. A fraction of 10% was observed in the irregular galaxy IC 10 by Madden et al. (1997), while Pineda et al. (2013) and Velusamy & Langer (2014) found that 20% of [C II] in the Milky Way arises from the CNM. A most recent study by Fahrion et al. (2017) found that only 9% of [C II] arises from CNM in a dwarf galaxy of NGC 4214.

6. Summary and Outlook

With an ionization potential of only 11.26 eV, C^+ can be found throughout the ISM. Its [C II] 157 μm fine-structure line provides one of the main cooling channels of the ISM. Since its strength correlates with the SFR density and is much less susceptible to dust extinction than other star formation tracers, it serves as an important diagnostic, although its accuracy is under discussion ("[C II] deficit").

The goal of this work was to establish an empirical multi-component model of the ISM to quantify the individual contributions of the various gas phases to the observed [C II] 157 μm emission. We defined five gas phases as follows: (1) dense H II regions, (2) the WIM, (3) dense PDRs, (4) low n_H and low G_0 SfMCs, and (5) the diffuse neutral medium (CNM/WNM).

To validate our model, we selected ten regions within the two nearby galaxies NGC 3184 and NGC 628 at distances of 11.6 Mpc and 9.5 Mpc, respectively. The main data were taken from the *Herschel* open time key program KINGFISH, and we combined them with a large set of ancillary photometric and spectroscopic data that were previously taken from the ground or by the *Spitzer Space Telescope*. Of the ten selected regions, three are located in NGC 3184 and seven in NGC 628. They comprise the two areas around the galactic nuclei as well as eight extra-nuclear regions. Our analysis was done at the resolution of the *Herschel* beam size, which corresponds to a physical size of 500–600 pc.

Our five-component ISM model reproduces the [C II] emission from the individual phases quite well. While the introduction of five ISM components and a wealth of ancillary data may at first sight introduce additional parameters into our model, our comprehensive approach also introduces another constraint: namely that the sum of the five phases must equal the total observed [C II] emission. We find that for most regions the sum of the modeled fluxes is within a factor of two of the total observed [C II] flux. Hence, we consider our results relatively reliable and accurate.

More specifically, our findings are as follows.

1. Our model of five ISM phases reproduces the observed [C II] in all regions to within a factor of two. On average, the sum of all individually and independently modeled components is about 45% higher than the observed [C II] flux, which is reassuringly close to the observed value.
2. The most important diagnostics in this context are density tracers of the WIM and H I 21 cm for the CNM. For dense PDRs a careful treatment of the gas tracers [O I] and H_2 is required.
3. Dense PDRs are the dominating component, contributing ~68% of the [C II] flux on average.
4. WIM and the SfMCs are the second strongest components with contributions of approximately half of the dense PDR contribution, respectively. The WIM is particularly strong in the nucleus of NGC 628, where it contributes most of the total observed [C II].
5. CNM and dense H II regions are only minor contributors with fractions of less than 5% on average.
6. The relative strength of all components varies significantly, depending on the physical properties of the gas. This variation provides the important physical basis for a subsequent analysis of a much larger sample of galaxies and regions.

The main uncertainties in the modeling of the H II region, the WIM, the dense PDR, the SfMC, and the CNM come from the uncertainties in electron density, n_e, G_0, the adopted densities and radiation fields, and the thermal pressure, respectively. While these uncertainties are inherent to all studies, it is sometimes difficult to compare numbers at face value. Many published [C II] contributions have been derived with different methods, and the systematic uncertainties are often not clearly stated. Nevertheless, our findings are in good agreement with specific studies in the literature. We should also keep in mind that despite the tremendous progress in this field that the *Herschel Space Telescope* has enabled, the angular resolution is still poor, with beam sizes corresponding to approximately 500 pc, which makes a direct comparison to studies of resolved regions within our Milky Way difficult.

As stated in Section 4.6, the main limitation with regard to generalizing our results to the entire galactic ISM is the selection bias toward regions with higher total infrared emission, i.e., ongoing massive star formation. While this bias is observationally unavoidable in spectroscopic studies of distant galaxies with the current generation of space observatories, it limits the applicability of our results to the ISM in more quiescent galactic regions. This selection bias is likely less relevant for more luminous galaxies, in particular those at cosmological distances, which suffer from similar selection biases.

In a subsequent paper we will apply our approach to a larger sample of galaxies and regions for a statistically more significant sample, making use of the comprehensive set of available ancillary data. In addition to KINGFISH, other *Herschel* programs such as the "Survey with *Herschel* of the ISM in Nearby Infrared Galaxies (SHINING)" (Sturm et al. 2011), and the "Dwarf Galaxy Survey (DGS)" (Madden et al. 2013) provide an excellent basis. Applying our model to a much larger galaxy sample will allow us to study the variations in gas physics and the resulting [C II] emission with higher statistical significance, leading to a thorough understanding of the origin of the [C II] emission across the universe.

We thank Fabian Rosales-Ortega, who provided unpublished PINGS data on NGC 3184 and helpful explanations on the reduction steps performed on NGC 3184. B.G. gratefully acknowledges the support of the Australian Research Council as the recipient of a Future Fellowship (FT140101202). PACS has been developed by a consortium of institutes led by MPE (Germany) and including UVIE (Austria); KU Leuven, CSL, IMEC (Belgium); CEA, LAM (France); MPIA (Germany); INAF-IFSI/OAA/OAP/OAT, LENS, SISSA (Italy); IAC (Spain). This development has been supported by the funding

agencies BMVIT (Austria), ESA-PRODEX (Belgium), CEA/CNES (France), DLR (Germany), ASI/INAF (Italy), and CICYT/MCYT (Spain).

Appendix
Deriving Gas Properties with an Analytical Calculation

A.1. The n_e, q, and Z Parameters

We investigate the parameter space of the electron density (n_e), metallicity (Z), and ionization parameter (q) using an analytical calculation. The electron density n_e, estimated from the doublet optical line [S II]6717,6731 ratio, ranges from 100 to 1500 cm^{-3}. We also used the MIR [S III]18, 33 for an independent estimate following the equation from (Watson & Storey 1980). The values of n_e as listed in Table 5 are calculated by averaging the n_e from both [S III] and [S II] lines. The densities derived from optical lines are in good agreement with the values found for extragalactic H II regions (Kennicutt 1984).

To calculate the ionization parameter (q), we follow the definition of Dopita et al. (2000), where $q = Q/(4\,\pi R_{\rm H\,II}^2 n_{\rm e})$, the ratio of ionizing photons per unit area per second over the number density of hydrogen atoms. We calculate the analytical H II region radius from q and n_e derived from MAPPINGS III modeling. Our calculation yields radii ranging from 2 to 8 pc, which is very small relative to the radius obtained from Gaussian fitting of the Hα images. This is due to our simple model assuming of all ionizing radiation arising from a single spherical H II region, while in reality, our selected regions likely comprise several H II regions (like in 30 Dor) that together provide the measured Hα profile. The discrepancy of analytical calculation and observational Hα does not affect the [C II] fraction from H II regions. However, our estimation of G_0 and consequently the [C II] emission from dense PDRs will be affected, as discussed in Appendix A.2. At any rate, the apparent discrepancy does not affect our overall conclusion that dense PDRs are the dominating [C II] contributor.

Since the metal abundances from Moustakas et al. (2010) are measured over a drift-scanned strip of galaxy, while we need the metallicity of each individual region, we decided to measure the metallicity in a different way. We used the two line ratios of [O III]5007/[O II] 3727, 3729 and [N II] 6548, 6584/[O II] 3727, 3729 to estimate the ionization parameter q and the metallicity Z with the photoionization code MAPPINGS III (Kewley et al. 2001; Dopita et al. 2000). Note that estimating the $\frac{[\rm N\,II]}{[\rm O\,II]}$ ratio required a certain assumption of the nitrogen/oxygen elemental abundance. We followed (Dopita et al. 2000) and assumed that nitrogen is a secondary nucleosynthesis element and does not scale linearly with increasing metallicity Z. We used the MAPPINGS 1 $Z_\odot$ metallicity set with C/H = 2.57 × 10^{-4}, N/H = 6.03 × 10^{-4}, and O/H = 4.57 × 10 − 4. For the 2 $Z_\odot$ metallicity we set C/H = 9.10 × 10^{-4}, N/H = 2.09 × 10^{-4}, and O/H = 9.10 × 10 − 4.

We find that Z and q vary by factors 1.7 and 1.5, respectively, when we change n_e by a factor of 3. A factor of 3 is taken to cover the range of density of extragalactic H II regions. These variations are less than the observational uncertainty in the line ratios. The derived metallicities for the four regions range from 1 $Z_\odot$ to 2 $Z_\odot$, in agreement with the study by Moustakas et al. (2010). The ionization parameters derived from the [O II], [O III], and [N II] lines are in accordance with the best-fit MAPPINGS model described in Section 4.1. We tabulate the metallicities and ionization parameters in Table 5.

A.2. Deriving G_0

We calculate G_0 of the ISM by three methods. The first method is by using the TIR luminosity. The basic assumption is that all UV radiation is converted by dust and re-emitted in the infrared. $L_{\rm TIR}$ is calculated following Equation (2) in Draine & Li (2007):

$$L_{\rm TIR} = 0.95\langle \nu S_\nu\rangle_8 + 1.15\langle \nu S_\nu\rangle_{24} + \langle \nu S_\nu\rangle_{70} + \langle \nu S_\nu\rangle_{160}, \quad (6)$$

and G_0 is calculated following Equation (7),

$$G_0 = \frac{L_{\rm (TIR/UV)}}{4\pi \times {R_{\rm H\,II}}^2 \times 1.6 \times 10^{-3}}, \quad (7)$$

where $L_{\rm TIR}$ is in erg s^{-1}, $R_{\rm H\,II}$ is the radius of the H II region (or, more precisely, the radius of the Hα emission region) in cm, and 1.6 × 10^{-3} is the Habing field in units of erg cm^{-2} s^{-1} (Tielens 2010). We used the size of the H II region to convert the observed $L_{\rm TIR}$ to the incident radiation field. We estimated the H II region radius via Gaussian fitting for regions with a distinct circular Hα structure and careful by-eye inspection for regions where the fitting fails. We found that the Hα emission is resolved for all of the regions. The radii of the H II regions range from 30 to 170 pc. The G_0 derived from $L_{\rm TIR}$ is in the range 30–530 (Table 5). We note that for some regions $L_{\rm TIR}$ is larger than $L_{\rm UV}$(6 regions in NGC 628 out of 7 regions). Older populations of stars may substantially contribute to the dust heating, as shown by Groves et al. (2012) and Draine et al. (2014), but not to the ionizing flux. Furthermore, we have made the simplifying assumption of spherical H II regions. Observations of Galactic as well as extragalactic H II regions amply illustrate that their PDR interfaces are highly corrugated, which can easily lead to an overestimation of the distance between the star clusters and the PDR surface.

As mentioned in Appendix A.2, the assumption of the geometry of the regions, i.e., the relative location of H II regions and dense PDRs, may affect our G_0 estimates. In our model we assume single H II regions with radius as listed in Table 5, and dense PDRs located adjacent to the H II region. Since we have no way of knowing the actual morphology of the regions, we adopt the simplest model as describe in Sections 4.1 and 4.3. If the the H II regions consist of several H II regions that are intermingled with the dense PDR, depending on the exact geometry, the G_0 is estimated to be higher than our current adopted value because the distance of H II regions and dense PDRs will be smaller. Increasing G_0 in turn will increase the [C II] fraction from dense PDRs.

The second method for estimating the incident radiation field emitted by the stellar cluster can be obtained from the ionizing photon luminosity as inferred from the extinction-corrected Hβ flux that is converted into NLyC and $L_{\rm UV}$. We have estimated the total stellar radiation field in the 6–13.6 eV range per ionizing photon using SB99 (Leitherer et al. 1999) assuming a continuous starburst for 10 million years, and derived G_0 from the above-described H II region radii. We find that G_0 derived from $L_{\rm UV}$ ranges between 8 and 180 (Table 5), which is two to three times smaller (on average) than the G_0 derived from $L_{\rm TIR}$. The third method is by using the dust model

of Draine & Li (2007) and Aniano et al. (2012), as explained in detail in Section 4.4.

References

Abel, N. P., Ferland, G. J., Shaw, G., & van Hoof, P. A. M. 2005, ApJS, 161, 65
Aniano, G., Draine, B. T., Calzetti, D., et al. 2012, ApJ, 756, 138
Aniano, G., Draine, B. T., Gordon, K. D., & Sandstrom, K. 2011, PASP, 123, 1218
Appleton, P. N., Guillard, P., Boulanger, F., et al. 2013, ApJ, 777, 66
Battisti, A. J., & Heyer, M. H. 2014, ApJ, 780, 173
Beirão, P., Armus, L., Helou, G., et al. 2012, ApJ, 751, 144
Bennett, C. L., Fixsen, D. J., Hinshaw, G., et al. 1994, ApJ, 434, 587
Berg, D. A., Skillman, E. D., Croxall, K. V., et al. 2015, ApJ, 806, 16
Bock, J. J., Hristov, V. V., Kawada, M., et al. 1993, ApJL, 410, L115
Boselli, A., Gavazzi, G., Lequeux, J., & Pierini, D. 2002, A&A, 385, 454
Braine, J., Combes, F., Casoli, F., et al. 1993, A&AS, 97, 887
Brauher, J. R., Dale, D. A., & Helou, G. 2008, ApJS, 178, 280
Burton, M. G., Hollenbach, D. J., & Tielens, A. G. G. 1992, ApJ, 399, 563
Carral, P., Hollenbach, D. J., Lord, S. D., et al. 1994, ApJ, 423, 223
Chevance, M., Madden, S. C., Lebouteiller, V., et al. 2016, A&A, 590, A36
Cormier, D., Lebouteiller, V., Madden, S. C., et al. 2012, A&A, 548, A20
Crawford, M. K., Genzel, R., Townes, C. H., & Watson, D. M. 1985, ApJ, 291, 755
Croxall, K. V., Smith, J. D., Brandl, B. R., et al. 2013, ApJ, 777, 96
Croxall, K. V., Smith, J. D., Wolfire, M. G., et al. 2012, ApJ, 747, 81
Dale, D. A., Aniano, G., Engelbracht, C. W., et al. 2012, ApJ, 745, 95
Dale, D. A., Gil de Paz, A., Gordon, K. D., et al. 2007, ApJ, 655, 863
de Looze, I., Baes, M., Bendo, G. J., Cortese, L., & Fritz, J. 2011, MNRAS, 416, 2712
De Looze, I., Fritz, J., Baes, M., et al. 2014, A&A, 571, A69
Díaz-Santos, T., Armus, L., Charmandaris, V., et al. 2013, ApJ, 774, 68
Dopita, M. A., Kewley, L. J., Heisler, C. A., & Sutherland, R. S. 2000, ApJ, 542, 224
Doran, E. I., Crowther, P. A., de Koter, A., et al. 2013, A&A, 558, A134
Draine, B. 2010, Physics of the Interstellar and Intergalactic Medium (Princeton, NJ: Princeton Univ. Press)
Draine, B. T., Aniano, G., Krause, O., et al. 2014, ApJ, 780, 172
Draine, B. T., & Li, A. 2007, ApJ, 657, 810
Fahrion, K., Cormier, D., Bigiel, F., et al. 2017, A&A, 599, A9
Fazio, G. G., Ashby, M. L. N., Barmby, P., et al. 2004, ApJS, 154, 39
Fitzpatrick, E. L. 1999, PASP, 111, 63
Gil de Paz, A., Boissier, S., Madore, B. F., et al. 2007, ApJS, 173, 185
Goldsmith, P. F., Yıldız, U. A., Langer, W. D., & Pineda, J. L. 2015, ApJ, 814, 133
Grier, C. J., Mathur, S., Ghosh, H., & Ferrarese, L. 2011, ApJ, 731, 60
Griffin, M. J., Abergel, A., Abreu, A., et al. 2010, A&A, 518, L3
Groves, B., Krause, O., Sandstrom, K., et al. 2012, MNRAS, 426, 892
Habart, E., Abergel, A., Boulanger, F., et al. 2011, A&A, 527, A122
Habing, H. J. 1968, BAN, 19, 421
Haffner, L. M., Dettmar, R.-J., Beckman, J. E., et al. 2009, RvMP, 81, 969
Heiles, C. 1994, ApJ, 436, 720
Heiles, C., & Troland, T. H. 2003, ApJ, 586, 1067
Heiner, J. S., Allen, R. J., & van der Kruit, P. C. 2011, MNRAS, 416, 2
Heiner, J. S., Sánchez-Gallego, J. R., Rousseau-Nepton, L., & Knapen, J. H. 2013, MNRAS, 428, 3355
Helou, G., Malhotra, S., Hollenbach, D. J., Dale, D. A., & Contursi, A. 2001, ApJL, 548, L73
Herrera-Camus, R., Bolatto, A., Smith, J. D., et al. 2016, ApJ, 826, 175
Herrera-Camus, R., Bolatto, A. D., Wolfire, M. G., et al. 2015, ApJ, 800, 1
Hills, R. E., & Beasley, A. J. 2008, Proc. SPIE, 7012, 70120N
Hollenbach, D. J., Takahashi, T., & Tielens, A. G. G. M. 1991, ApJ, 377, 192
Hollenbach, D. J., & Tielens, A. G. G. M. 1997, ARA&A, 35, 179
Houck, J. R., Roellig, T. L., van Cleve, J., et al. 2004, ApJS, 154, 18
Ingalls, J. G., Bania, T. M., Boulanger, F., et al. 2011, ApJ, 743, 174
Ingalls, J. G., Reach, W. T., & Bania, T. M. 2002, ApJ, 579, 289
Jenkins, E. B., & Tripp, T. M. 2011, ApJ, 734, 65
Kapala, M. J., Sandstrom, K., Groves, B., et al. 2015, ApJ, 798, 24
Kaufman, M. J., Wolfire, M. G., & Hollenbach, D. J. 2006, ApJ, 644, 283
Kelz, A., Verheijen, M. A. W., Roth, M. M., et al. 2006, PASP, 118, 129
Kennicutt, R. C., Calzetti, D., Aniano, G., et al. 2011, PASP, 123, 1347
Kennicutt, R. C., Jr. 1984, ApJ, 287, 116
Kennicutt, R. C., Jr., Armus, L., Bendo, G., et al. 2003, PASP, 115, 928
Kennicutt, R. C., Jr., Hao, C.-N., Calzetti, D., et al. 2009, ApJ, 703, 1672
Kennicutt, R. C., Jr., Keel, W. C., & Blaha, C. A. 1989, AJ, 97, 1022
Kewley, L. J., Dopita, M. A., Sutherland, R. S., Heisler, C. A., & Trevena, J. 2001, ApJ, 556, 121
Kraemer, K. E., Jackson, J. M., & Lane, A. P. 1998, ApJ, 503, 785
Kramer, C., Mookerjea, B., Bayet, E., et al. 2005, A&A, 441, 961
Lebouteiller, V., Cormier, D., Madden, S. C., et al. 2012, A&A, 548, A91
Lebouteiller, V., Heap, S., Hubeny, I., & Kunth, D. 2013, A&A, 553, A16
Leitherer, C., Schaerer, D., Goldader, J. D., et al. 1999, ApJS, 123, 3
Leroy, A. K., Bigiel, F., de Blok, W. J. G., et al. 2012, AJ, 144, 3
Leroy, A. K., Walter, F., Bigiel, F., et al. 2009, AJ, 137, 4670
Leurini, S., Wyrowski, F., Wiesemeyer, H., et al. 2015, A&A, 584, A70
Luhman, M. L., Satyapal, S., Fischer, J., et al. 1998, ApJL, 504, L11
Luhman, M. L., Satyapal, S., Fischer, J., et al. 2003, ApJ, 594, 758
Madden, S. C., Geis, N., Genzel, R., et al. 1993, ApJ, 407, 579
Madden, S. C., Poglitsch, A., Geis, N., Stacey, G. J., & Townes, C. H. 1997, ApJ, 483, 200
Madden, S. C., Rémy-Ruyer, A., Galametz, M., et al. 2013, PASP, 125, 600
Malhotra, S., Kaufman, M. J., Hollenbach, D., et al. 2001, ApJ, 561, 766
Martin, D. C., Seibert, M., Buat, V., et al. 2005, ApJL, 619, L59
Mathis, J. S., Mezger, P. G., & Panagia, N. 1983, A&A, 128, 212
Matsuhara, H., Tanaka, M., Yonekura, Y., et al. 1997, ApJ, 490, 744
Mizutani, M., Onaka, T., & Shibai, H. 2004, A&A, 423, 579
Monnet, G. 1971, A&A, 12, 379
Mookerjea, B., Kramer, C., Buchbender, C., et al. 2011, A&A, 532, A152
Moustakas, J., Kennicutt, R. C., Jr., Tremonti, C. A., et al. 2010, ApJS, 190, 233
Nakagawa, T., Doi, Y., Yui, Y. Y., et al. 1995, ApJL, 455, L35
Oberst, T. E., Parshley, S. C., Stacey, G. J., et al. 2006, ApJL, 652, L125
O'Dell, C. R., Ferland, G. J., Porter, R. L., & van Hoof, P. A. M. 2011, ApJ, 733, 9
Orr, M. E., Pineda, J. L., & Goldsmith, P. F. 2014, ApJ, 795, 26
Ossenkopf, V., Koumpia, E., Okada, Y., et al. 2015, A&A, 580, A83
Osterbrock, D., & Ferland, G. 2006, Astrophysics of Gaseous Nebulae and Active Galactic Nuclei (Mill Valley, CA: Univ. Science Books)
Ott, S. 2010, in ASP Conf. Ser. 434, Astronomical Data Analysis Software and Systems XIX, ed. Y. Mizumoto, K.-I. Morita, & M. Ohishi (San Francisco, CA: ASP), 139
Parmar, P. S., Lacy, J. H., & Achtermann, J. M. 1991, ApJL, 372, L25
Pierini, D., Leech, K. J., Tuffs, R. J., & Volk, H. J. 1999, MNRAS, 303, L29
Pilbratt, G. L., Riedinger, J. R., Passvogel, T., et al. 2010, A&A, 518, L1
Pineda, J. L., Langer, W. D., & Goldsmith, P. F. 2014, A&A, 570, A121
Pineda, J. L., Langer, W. D., Velusamy, T., & Goldsmith, P. F. 2013, A&A, 554, A103
Poglitsch, A., Waelkens, C., Geis, N., et al. 2010, A&A, 518, L2
Pound, M. W., & Wolfire, M. G. 2008, in ASP Conf. Ser. 394, Astronomical Data Analysis Software and Systems XVII, ed. R. W. Argyle, P. S. Bunclark, & J. R. Lewis (San Francisco, CA: ASP), 654
Reynolds, R. J. 1991, ApJL, 372, L17
Reynolds, R. J., Chaudhary, V., Madsen, G. J., & Haffner, L. M. 2005, AJ, 129, 927
Rodriguez-Fernandez, N. J., Braine, J., Brouillet, N., & Combes, F. 2006, A&A, 453, 77
Röllig, M., Simon, R., Güsten, R., et al. 2016, A&A, 591, A33
Rosales-Ortega, F. F., Kennicutt, R. C., Sánchez, S. F., et al. 2010, MNRAS, 405, 735
Roussel, H. 2013, PASP, 125, 1126
Roussel, H., Helou, G., Hollenbach, D. J., et al. 2007, ApJ, 669, 959
Rubin, R. H. 1984, ApJ, 287, 653
Salpeter, E. E. 1955, ApJ, 121, 161
Sánchez, S. F., Rosales-Ortega, F. F., Kennicutt, R. C., et al. 2011, MNRAS, 410, 313
Sargsyan, L., Lebouteiller, V., Weedman, D., et al. 2012, ApJ, 755, 171
Sargsyan, L., Samsonyan, A., Lebouteiller, V., et al. 2014, ApJ, 790, 15
Sembach, K. R., Howk, J. C., Ryans, R. S. I., & Keenan, F. P. 2000, ApJ, 528, 310
Sheffer, Y., & Wolfire, M. G. 2013, ApJL, 774, L14
Sheffer, Y., Wolfire, M. G., Hollenbach, D. J., Kaufman, M. J., & Cordier, M. 2011, ApJ, 741, 45
Shibai, H., Okuda, H., Nakagawa, T., et al. 1991, ApJ, 374, 522
Shields, G. A. 1990, ARA&A, 28, 525
Smith, J. D. T., Armus, L., Dale, D. A., et al. 2007a, PASP, 119, 1133
Smith, J. D. T., Croxall, K., Draine, B., et al. 2017, ApJ, 834, 5
Smith, J. D. T., Draine, B. T., Dale, D. A., et al. 2007b, ApJ, 656, 770
Stacey, G. J., Geis, N., Genzel, R., et al. 1991, ApJ, 373, 423
Stacey, G. J., Hailey-Dunsheath, S., Ferkinhoff, C., et al. 2010, ApJ, 724, 957
Stacey, G. J., Jaffe, D. T., Geis, N., et al. 1993, ApJ, 404, 219

Stacey, G. J., Viscuso, P. J., Fuller, C. E., & Kurtz, N. T. 1985, ApJ, 289, 803
Sturm, E., Poglitsch, A., Contursi, A., et al. 2011, EAS Publications Ser., 52, 55
Tielens, A. 2010, The Physics and Chemistry of the Interstellar Medium (Cambridge: Cambridge Univ. Press)
Tielens, A. G. G. M., & Hollenbach, D. 1985, ApJ, 291, 722
Tielens, A. G. G. M., Hony, S., van Kerckhoven, C., & Peeters, E. 1999, in The Universe as Seen by ISO, ed. P. Cox & M. Kessler (Noordwijk: ESA), 579
Tufte, S. L., Reynolds, R. J., & Haffner, L. M. 1998, in ASP Conf. Ser. 141, Astrophysics From Antarctica, ed. G. Novak & R. Landsberg (San Francisco, CA: ASP), 169
Vasta, M., Barlow, M. J., Viti, S., Yates, J. A., & Bell, T. A. 2010, MNRAS, 404, 1910
Vastel, C., Spaans, M., Ceccarelli, C., Tielens, A. G. G. M., & Caux, E. 2001, A&A, 376, 1064
Velusamy, T., & Langer, W. D. 2014, A&A, 572, A45
Velusamy, T., Langer, W. D., Pineda, J. L., & Goldsmith, P. F. 2012, A&A, 541, L10
Walter, F., Brinks, E., de Blok, W. J. G., et al. 2008, AJ, 136, 2563
Watson, D. M., & Storey, J. W. V. 1980, IJIMW, 1, 609
Werner, M. W., Roellig, T. L., Low, F. J., et al. 2004, ApJS, 154, 1
Wiesemeyer, H., Güsten, R., Heyminck, S., et al. 2016, A&A, 585, A76
Wolfire, M. G., Hollenbach, D., McKee, C. F., Tielens, A. G. G. M., & Bakes, E. L. O. 1995, ApJ, 443, 152
Wolfire, M. G., McKee, C. F., Hollenbach, D., & Tielens, A. G. G. M. 2003, ApJ, 587, 278
Wright, E. L., Mather, J. C., Bennett, C. L., et al. 1991, ApJ, 381, 200